Doctoral Dissertation

Optimization of Chemical Composition of *p*-type Filled-Skutterudites for Enhancement of Thermoelectric Properties

熱電特性向上のための *p* 型充填スクッテルダイトの化学組成最適化

JUNGMIN KIM

January 2019

Graduate School of Engineering

Osaka University

Thesis Advisors:

Associate Professor Ken Kurosaki, Ph.D.

Kurosaki-Muta Laboratory, Division of Sustainable Energy and Environmental Engineering,

Graduate School of Engineering, OSAKA UNIVERSITY

Thesis Committee:

Associate Professor Ken Kurosaki, Ph.D.

Professor Yamamoto Takao, Ph.D.

Professor Takanori Kitada, Ph.D.

Associate Professor Hiroaki Muta, Ph.D.

Graduate School of Engineering

OSAKA UNIVERSITY

Abstract

Thermoelectric power generation (TEG) is essential in new/renewable energy conversion technology to solve the global environmental pollution and energy crisis, which have been developed in high tech applications such as spacecraft and also have been recently applied in a variety of fields such as car engine and watch. The performance of thermoelectric (TE) device depends on the type of materials used and properties such as their thermal conductivity, Seebeck coefficient, electrical conductivity, and thermal stability etc. Among the various TE materials, skutterudite have received attention as promising material due to the high TE performance and good mechanical properties. However, *p*-type skutterudites have lower TE properties than the *n*-type ones, therefore to improve high efficiency of TEG device, higher performance of *p*-type ones are required.

The purpose of this thesis is to enhance TE properties of *p*-type $CoSb_3$-based skutterudites. The another one is to confirm that behavior of introduced and substituted various elements (In, Ce, Ga, Fe) in the skutterudite main phase.

In the chapter I and II, we introduced the background of thermoelectric with essentially theoretical concepts and summarizes the experimental methods and characterize the material investigated used in this thesis. Especially, in the chapter II, we described the the sintering techniques and measurement techniques applied to confirm the material properties.

In the chapter III, thermoelectric properties of In single-filled *p*-type $In_xFeCo_3Sb_{12}$ were examined. All the synthesized samples showed *p*-type conduction of Seebeck coefficient. The filling fraction of obtained samples was indicated that is extended to the value of $x = 0.43$. I confirmed that the increase of the In led to the reduction carrier concentration, because In provided the system with conduction electrons through the results of Hall measurement. As a result, the reduced lattice thermal conductivity caused by the rattling effect of filled In and the enhanced PF with an appropriate hole concentration led to large magnitude values of zT .

In the chapter IV, we investigated Ce-filled (Co, Fe)Sb_3 as *p*-type $Ce_xFe_yCo_{4-y}Sb_{12}$. The samples ($x = 0.8$, 0.9, 1.0 and $y = 3.0$, 3.5) are synthesized and their TE properties are examined, which obtained all samples indicate the *p*-type conduction. Consequently, I revealed that the carrier concentration can be control by optimization of substituted Fe and filled Ce. Especially, results of this study mean that the substituted Fe is more effective than the filled Ce for the reduction of thermal conductivity.

In the chapter V, we try to improve the TE properties of Ce-filled (Co, Fe)Sb_3 by co-filling of Ga. The samples $Ga_xCeFe_{3.5}Co_{0.5}Sb_{12-x/3}$ in the nominal composition are synthesized and their TE properties are examined. It is revealed that the Ga contributed to optimize the carrier concentration as well as to decrease the lattice thermal conductivity. Furthermore, we confirmed

that the Ga occupy not only the void site but also the Sb site. Owing to these Ga contributions, the material's TE properties are enhanced.

In summary, the effect of various filler atoms (In, Ce, Ga) and substituted Fe on the TE properties was compared experimentally. I confirmed that it is possible to optimize the carrier concentration tuning the filler/substituted atoms. Furthermore, in case of (Fe, Co)Sb_3, substituted Fe/Co is more effective than the filled atom for the reduction of lattice thermal conductivity. Consequentially, I could enhance the TE properties of *p*-type skutterudites through the optimization of chemical composition.

The results in each of the studies discussed will provide valuable insight into the role of enhancement of TE properties in their various applications and can apply to environmental, thermoelectric designs for the development of high-performance TEG materials.

TABLE OF CONTENTS

CHAPTER Page

CHAPTER Page

CHAPTER I

Introduction

1.1 Background and Motivations

Most the electricity energy that we use today are generated from fossil fuels. However, over the last few decades, with decreasing the amounts of reserved fossil fuels and increasing the environmental pollution such as green-house effect, significance of the renewable resources of energy such as wind, solar, bio energy, and clean transportation, etc. is getting bigger for resolving the today's energy crisis. In general, the global energy use relies on thermal processes, over 40 ~ 70 % of the energy used in factory, automobile, building, etc. is wasted on energy loss or waste heat [1]. In this point of view, renewable energy conversion technologies such as solar cell, fuel cell, and thermoelectric generation (TEG) have been regarded as alternative technology for conventional generation, although their application is limited due to their high cost, poor stability. Thermoelectric (TE) generators can directly convert waste heat into electricity in a variety of application including building heating, automobile exhaust and industrial production process. Furthermore, TE generators are extremely simple, have no moving parts, also they are silent, scalable and reliable power generation [2].

Despite all these advantages, required to improve the TE conversion efficiency with the TE material converts heat into electricity for practical use. Especially, the energy conversion efficiency of TE devices is very low compared to the other renewable energy resources as shown in Fig. 1.1 Since the 1990s, theoretical researches suggested that TE conversion efficiency could be greatly enhanced through using nano-structural engineering, which led to variety researches to discover the high-efficiency TE materials as shown Fig. 1.2. [3] Although a high efficiency has been reported in the state of the art TE materials, many of these materials are impossible to practical for commercial use because they are complex to fabricate, slow and expensive.

For commercial use of TE material, bulk materials such as clathrates and skutterudites have been investigated and found that high efficiency could be obtained. Although, *n*-type bulk TE materials have high value of a figure of merit (zT) about 1.5, but *p*-type bulk TE materials still have low value of zT less 0.8. Thus, for various commercial use of TE technology, enhancement of TE properties is absolutely required for *p*-type TE bulk materials.

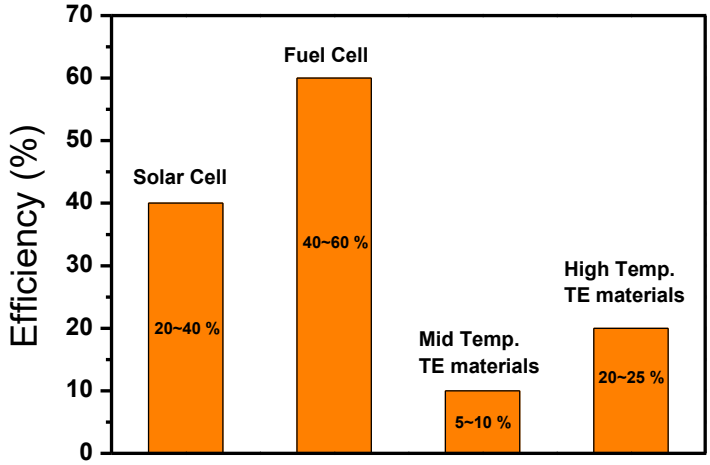

Fig. 1.1. The energy conversion efficiency by various generation technologies [2].

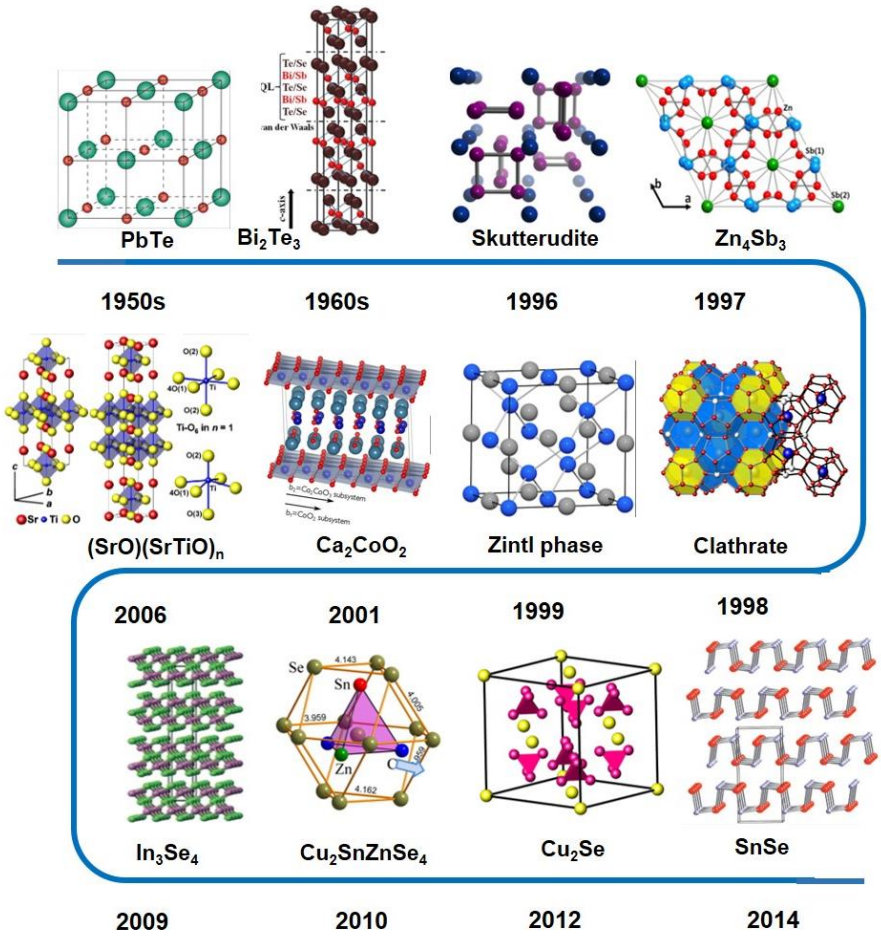

Fig. 1.2. The development of thermoelectric materials [3].

1.2 Introduction of Thermoelectric

1.2.1 Thermoelectric Phenomena

In 1821, Seebeck had discovered a potential difference caused by heating the junctions between the another conductor. Fig. 1.3 represents the schematic of Seebeck effect. The Seebeck coefficient is defined as the ratio of temperature gradient and potential difference, also known as the thermopower *S* as shown Eq. (1-1).

$$S = \lim_{\Delta T \to 0} \frac{\Delta V}{\Delta T} \tag{1-1}$$

The principle of Seebeck effect can be explained that high kinetic energy carrier on the hot side diffuse to the lower carrier energy region on cold side as shown in Fig. 1.4. The sign (positive or negative) of the Seebeck coefficient represents the major carrier type of used material.

In 1834, Peltier discovered another thermoelectric effect as shown in Fig. 1.3(b). When electricity current passes through a junction of two dissimilar metals there is generation or absorption of heat. As shown in Eq. (1-2) the Peltier coefficient (Π_{ab}) is defined as the rate of reversible heat generation Q over the current I passing through the junction.

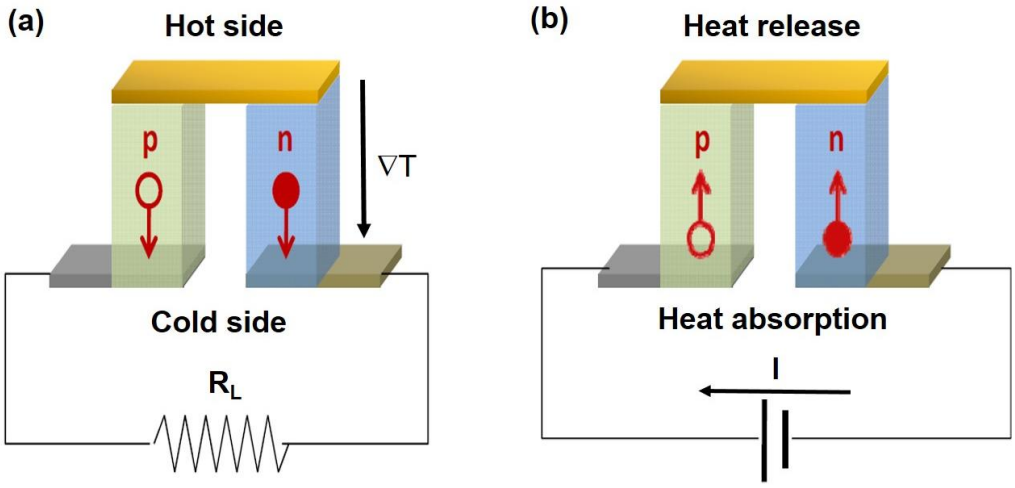

Fig. 1.3. Schematic illustration for Seebeck effect (a) and Peltier effect (b).

$$\Pi_{ab} = \frac{Q}{I} \tag{1-2}$$

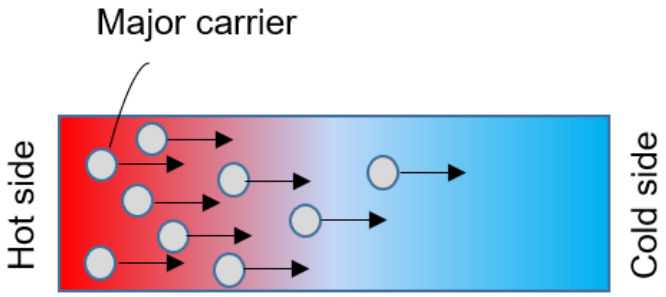

Fig. 1.4. Schematic illustration for the movement of carriers.

1.2.2 Dimensionless figure of merit

Thermoelectric (TE) devices offer a possibility to directly convert waste heat into electricity (TE generator), thus providing a promising solution to increase the efficiency of the energy usage in the future. The performance of a TE device is represented by the dimensionless figure of merit (zT), which depends on the electrical conductivity (σ), Seebeck coefficient (S) and the thermal conductivity (κ). In here, thermal conductivity represents the $\kappa = \kappa_e + \kappa_{lat}$, where κ_e is the thermal conductivity of the charge carriers and κ_{lat} is the thermal conductivity of the lattice phonons. And also, electrical conductivity represents the $\sigma = n\mu e$, where n is the charge carrier concentration, μ is the charge carrier mobility and e is the elementary charge (1.602×10^{-31} C).

$$zT = \frac{\sigma S^2}{\kappa} T \qquad (1\text{-}3)$$

The combination of terms in Eq. (1-3) already defines the optimization routes to obtain high zT materials: unfortunately, all three main parameters are interdependent, therefore any optimization has to find the best compromise. S and σ are inter-linked via charge carrier density (n) by Mott's formula [4]:

$$S = \frac{2\pi^2 k_B m_e}{|e|h^2(3n\pi^2)^{2/3}} T \qquad (1\text{-}4)$$

Where me is the electron mass (9.11×10^{-31} kg), h is the reduced Planck's constant (1.055×10^{-34} Js), and k_B is the Boltzmann constant (1.38×10^{-23} J/K). σ and κ are partially connected via the Wiedemann-Franz law [5]:

$$\kappa_e = \frac{L}{\rho} T \qquad (1\text{-}5)$$

Where L is the Lorenz number ($L_0 = 2.45 \times 10^{-8}$ WΩK^{-2} for metals and degenerate semiconductor)

The overall efficiency (η) of a TE generator device depends also on the temperature gradient between the hot (T_H) and the cold side (T_C) as proposed by Ioffe [6]:

$$\eta = \frac{T_H - T_C}{T_H} \frac{\sqrt{zT_{av}+1}}{\sqrt{zT_{av}+1}+\frac{T_C}{T_H}} \qquad (1\text{-}6)$$

involving zT_{av}, which is the average zT in the temperature interval of the T gradient supplied. In Fig. 1.5, the effects of zT for the TE conversion efficiency are showed. In here, the TE conversion efficiency for zT value of around 1 is ~15 % and for zT value around 3 is ~ 25 %. The zT values over 2, have been achieved already with the state of the art TE materials currently in use.

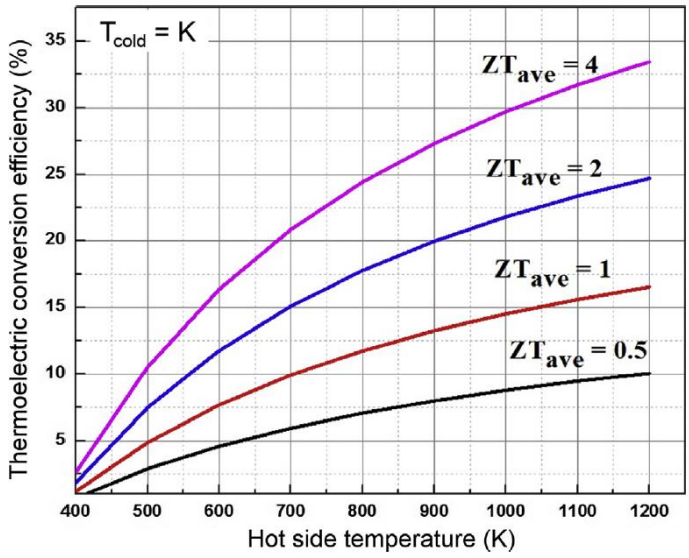

Fig. 1.5. Temperature dependent TE conversion efficiency [7].

1.2.3 Carrier Concentration

The amounts of majority carriers in TE material determined the electrical properties as well as Seebeck coefficient. Therefore, TE studies require the majority carrier concentration to be optimized for prevent decrease the electrical properties due to the bipolar conduction. In general, hall effect measurement are used to determine the carrier type, mobility, and major carrier concentration in semiconductors of TE materials [8]. The majority carrier concentration and the intrinsic property of the dopant further affects the carrier type and majority carrier concentration of TE material. Especially the majority carrier concentration determines both the electrical

conductivity and Seebeck coefficient as shown in Fig. 1.6 [9]. And also, carrier concentration of TE material is determined by the major carrier concentration doping elements, and temperature.[10] Experimentally, it have been found that with increasing temperature, the carrier concentration is increase. And also, the major carrier mobility act significant role in
determining electrical conductivity. The mobility of TE material can be change by various factor such as doping, alloying, impurity, grain boundaries, ratio of secondary phases, sample density, etc.

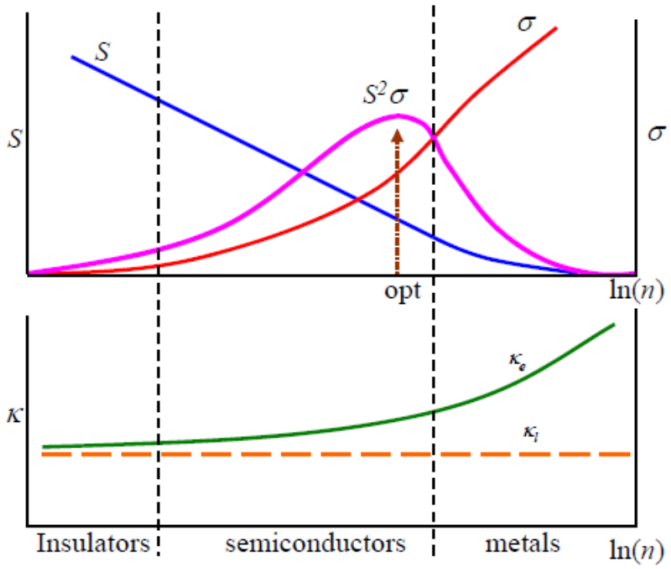

Fig. 1.6. The TE properties of various material as a function of carrier concentration [11].

1.2.4 Seebeck Coefficient

In TE materials, the Mott equation represents the Seebeck coefficient (*S*) as shown Eq. (1-7):

$$S = \frac{\pi^2}{3}\frac{k_B}{q}k_B T\left(\frac{1}{n}\frac{dn(E)}{dE} + \frac{1}{\mu}\frac{d\mu(E)}{dE}\right)_{E=E_F} \qquad (1\text{-}7)$$

In here, n(E) represents the density of charge carrier at energy level E, μ(E) represent the mobility of charge carrier at energy level E and E_F shows the Fermi energy level, and q shows the electronic charge. For high efficiency of TE conversion, TE material need to have a high *S* (>150 μV/K), this means that the good voltage-generating ability.[12] In general, the *S* depends on the bandgap of its material and their carrier concentration. And also, the *S* dependent on absolute temperature, majority carrier concentration, chemical composition, and crystal structure of the TE material. In

TE module, when given a temperature difference, it generates charge carrier. That is, generated charge carrier (electrons or holes) diffuse from the hot region to the cold region in a TE module. When measuring *S*, we should be aware of the follows: 1) we should be measured both temperature difference and current voltage at the same time in steady state system, 2) temperature gradient for the measured voltage should be linearly response, and 3) at the same measuring point, we should be measured the *S*. In general, among the materials (metal, insulator, and semiconductor), metal shows the lowest value of *S* (~ 10 μV/K) and insulator shows the highest value of *S* (> 200μV/K). In TE material, the efficiency of TE conversion depend on the *S* or thermo-power, thus, we can obtain the highest TE conversion efficiency at the large temperature gradient. There are many strategies to enhance the *S* as follows: 1) one is to increase the μ(E) by using the scattering mechanism 2) another one is to increase the *n*(E) [13].

1.2.5 Electrical Conductivity

For semiconductor, the electrical conductivity (σ) depend on charge carrier concentration and charge carrier mobility as shown in Eq. (1-8):

$$\sigma = e\left(\mu_e \cdot n \quad + \mu_h \cdot p\right) \tag{1-8}$$

In where, μ_e represent the electron mobility and μ_h represent the hole mobility and n, p represent the electron density, and hole density, respectively. Table 1.1 shows the electrical properties of TE materials, as shown in this figure, semiconductor TE materials have good electrical conductivity and Seebeck coefficient. Various scattering mechanism (such as lattice or impurity) determine the majority carrier mobility (electron and hole). In semiconductors TE material, impurities can affect the majority carrier mobility. Contrary to the lattice scattering, the impurity scattering decreases with increasing temperature which led to increase the carrier mobility. The electrical conductivity of TE materials can be influenced by various factor (such as temperature, doping, type of material, and impurities). Furthermore, there have been revealed that the electrical conductivity is influenced from structural parameters (such as strain, lattice constant, and grain size) [14,15].

Table. 1.1. Electrical properties of various materials at room temperature [16].

Property	Metals	Semiconductor	Insulator
S (μVK^{-1})	~ 5	~ 200	~ 1000
σ(Ω^{-1}cm^{-1})	~ 10^{6}	~ 10^{3}	~ 10^{-12}

1.2.6 Thermal Conductivity

Total thermal conductivity is consisted of two parameter charge carrier thermal conductivity and lattice (phonon) thermal conductivity. That is, total thermal conductivity (κ) represents this equation $\kappa = \kappa_e + \kappa_{lat}$, which is the sum of the electrical thermal conductivity (κ_e) and lattice thermal conductivity (κ_{lat}).[16] The thermal conductivity contributed by majority carrier (κ_e) can be calculated from the Wiedemann-Franz equation ($\kappa_e = L\sigma T$), in where L, σ, and T indicate Lorenz number, electrical conductivity, and absolute temperature respectively. Lorenz number of metal is ~ 2.45 × 10^{-8} V^2K^{-2} and ~ 1.5 × 10^{-8} V^2K^{-2} for semiconductor. And also, lattice thermal conductivity represents Eq. (1-9) as follows:

$$\kappa_{lat} = \rho \cdot C_p \cdot d \qquad (1\text{-}9)$$

In here, ρ, Cp, and d represent electrical resistivity, specific heat, and density of TE material respectively. In the research for TE material, the measurement of their thermal conductivity is a powerful method to enhance the thermal properties due to investigating imperfections or lattice defects of TE material. Heat move in solids through the phonon, charge carrier (electron and hole), spin wave, and electromagnetic wave or excitations. When the electron's charge carrier concentration and mobility are comparable to that of holes, bipolar diffusion (bipolar effect) can decrease the charge carrier thermal conductivity. Using Eq. (1-10) involved bipolar term, we can calculate the electrical lattice thermal conductivity. In where, k_B, E_g, μ_e, μ_h represent the Boltzmann constant, band gap energy, electron mobility, and hole mobility of TE material, respectively.

$$\kappa_e = \sigma T\left(\frac{k_B}{e}\right)^2 \left[2 + \left(4 + \frac{E_g}{k_B T}\right)^2 \frac{\mu_e/\mu_h}{(1+\mu_e/\mu_h)^2}\right] \qquad (1\text{-}10)$$

The phonon generated by lattice vibration strongly affect the charge carrier (electron and

hole) mobility. Thus, lattice thermal conductivity is influenced by lattice parameters and crystal structure of TE material. Various parameters (such as density, lattice constant, and anharmonic lattice) affect lattice thermal conductivity according to Eq. (1-11), where a, γ, h, and θ_D are lattice constant, Gruneisen parameter, Planck's constant, and Debye temperature respectively. In here, Gruneisen parameter means anharmonicity of lattice vibration. And also, for alloying compounds, the composition of compounds influence on lattice thermal conductivity due to the variation in their lattice constant. Thus, the technique of doping and alloying can be control lattice constant of TE material and reduce the lattice thermal conductivity.

$$\kappa_{lat} = \frac{{k_B}^3}{h^3}\frac{a^4 \rho \theta_D^3}{\gamma^2 T} \tag{1-11}$$

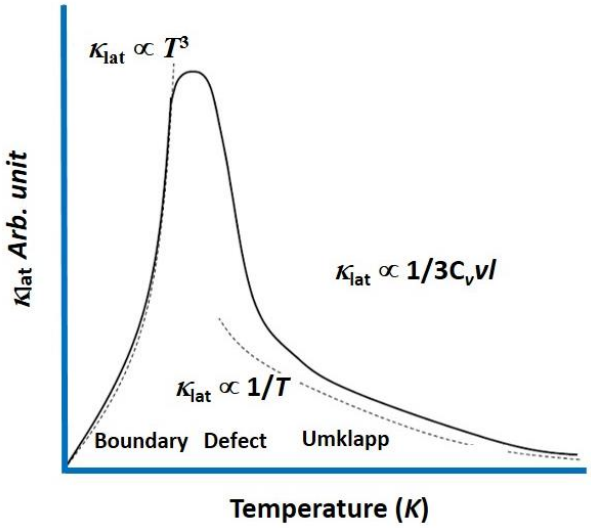

Fig. 1.7. Scattering mechanism in lattice thermal conductivity [19].

As I mentioned above, we can be improved the TE performance by reduction of thermal conductivity. Figure 1.7 shows the temperature dependence of scattering mechanism in lattice thermal conductivity. The lattice thermal conductivity is not influenced parameter from electrical properties in TE properties. Thus, there are many results of researches about reducing lattice thermal conductivity. In general, the thermal conductivity of lattice term can be express by $\kappa_{lat} = 1/C_v vl$, where Cv, v, and l are heat capacity, phonon velocity and phonon mean free path respectively.

When the dimension of defects or inclusions is comparable to the mean free path of phonon, the phonon can be effectively scattered in solid. The most heat is carried by acoustic phonon in material, which have wide wavelength range and mean free path distribution, including from short to long wavelength phonon. Thus, we can reduce the lattice thermal conductivity using the structural control such as grain boundary, nano precipitates, and solid solution point defect control as shown in Fig. 1.8. We can form the point defect in the material using the doping and allying method, which can reduce the lattice thermal conductivity. They are explained by Callaway model *via* the mass fluctuations (mass difference) and the stain field fluctuations (interatomic force difference between the host lattice and the impurity atom).[20] Nano-inclusions can be obtained by several approaches, dispersing oxidized nano-particles, including embedded nano-inclusions, and the endotaxial nano-precipitates.[21,22]

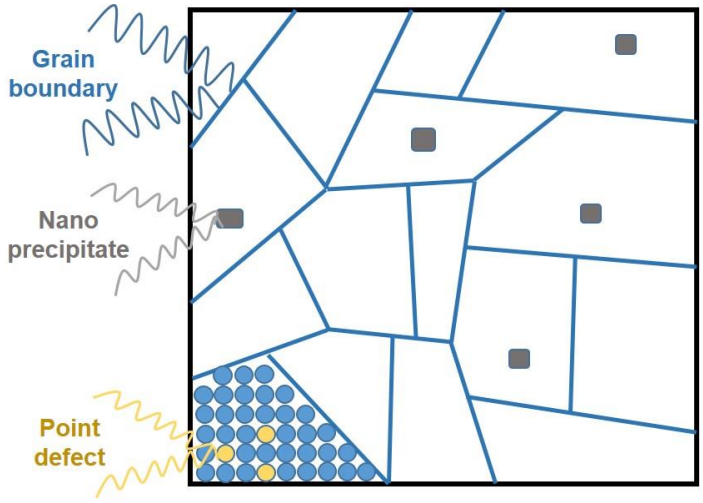

Fig. 1.8. Various phonon scattering effect for zT [23].

1.3 The Strategies to Improve the Thermoelectric Properties

1.3.1 Doping

Only the selecting of the suitable dopant atoms, we can enhance the carrier concentration of TE material by tuning their electronic band structure. Thus, the DOS of the TE materials are converted as the number of states per energy is increased with more addition of the suitable dopant atoms. The energy states near the Fermi energy level within an k_BT can cause the electron transport.

Thus, at an optimal majority carrier concentration, a higher Seebeck coefficient or zT value can be obtained for semimetals and semiconductor. And also, the values of maximum zT can be obtained when 1) Fermi energy and conduction band is closer, and 2) when the degeneracy of material is not strong. In these case, $E < E_F$ or $E > E_F$ majority charge carriers are highly asymmetric in terms of their DOS and contribution [24,25]. With an increase in majority carrier concentration of TE material, the Fermi energy level exceeds k_BT, which affects the thermopower negatively.

For inhancing the power factor (PF) of TE materials, we can use doping of element such as modulation doping and uniform dopoing due to the changing the carrier concentration. Through this method, we can obtain the higher electrical properties of TE materials. Various heveay doped TE materials show exelent PF values than its low or undoped ones [26, 27]. For instance, among the bulk TE materials, Seebeck coefficient of PbTe can enhance without reduction of the electrical conductivity due to the changing DOS of electron by doping control. And also, these band engineering method such as modulation dopoing enhances the carrier mobility by decreasing inized point scattering because the carriers are divided from major grain into undoped grains [28]. Furthermore, using the carrier pocket engineering we can cause the convergence of electronic bands in the TE bulk material with high valley degeneracy [29]. As a result, this convergence of the conduction and valance bands of electron enhence both the electrical conductivity and Seebeck coefficient values [29].

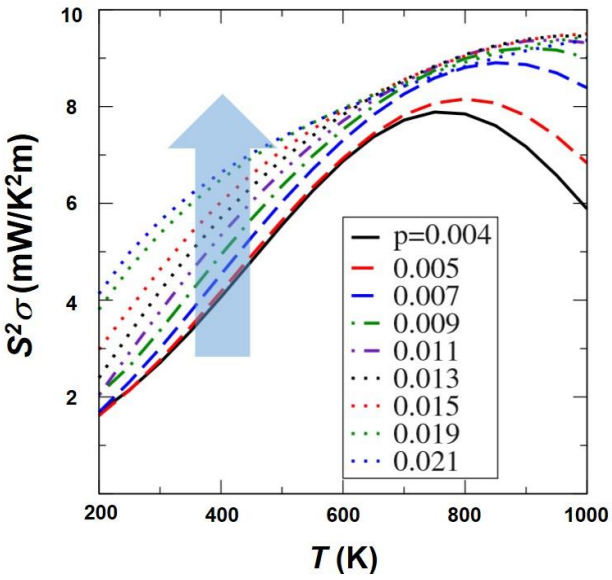

Fig. 1.9. The Calculated power factor for doped PbSe at various carrier concentration [26].

For enhancing *zT*, the doping of modulation or impurity due to the precipitate of anti-resonance nano-size particles into the parent grain can be an attractive method. Band offset of electron and optimization of effective mass are used, which enhance the *PF* values of TE materials by effect of scattering carrier. Through the using these methods, we can enhance both the Seebeck coefficient and electrical conductivity of the TE materials with anti-resonance nano-size particles. Furthermore, there is a large acoustic mismatch between the host material and the nano size particle with core-shell, which decrease the lattice thermal conductivity without reduction of the *PF* [30]. In some of cases, dopant energy levels of the TE materials can make resonant energy levels, and also, these energy levels can change the DOS of electron close to the Fermi level. Therefore, the effective mass for the TE materials can be enhanced without affecting the charge carrier concentration, for instance, Cr in PbTe or Tl in PbTe. These are important for enhancing the Seebeck coefficient and also which is dependent on the doping concentration. The large change in the DOS of electron near the impurity band can enhance the *PF* of TE materials as shown in Figure 1. 10. Which enhances the major carrier effective mass without affecting the carrier concentration of TE materials, in other words, only the Seebeck coefficient is enhanced without changing the electrical conductivity [31]. While, for parabolic band with non-degenerate charged carrier, if the bandgap is largely greater than k_BT, and then the minority carrier concentration or their act of charge transport can become negligible. In here, width of the bandgap and Fermi level around the bottom of the conduction band are responsible, therefore largely enhancing the *PF* of the TE material. Thus, this gap become greater than the temperature for given temperature, for example, Eg > 10 k_BT [32,33]. Bands of electron are congregated by changing doping or chemical composition of TE bulk materials. Many valley degeneracy is an ideal property for the TE materials [35]. Therefore, the separation of pockets for Fermi surface with the multiple degenerate valleys can become a large effective mass of DOS without reduction of the carrier mobility. In here, the electrical properties depend on the weighted carrier mobility $\mu \cdot (m^*/m_e)^{3/2}$, where μ is charge carrier mobility, m* is the effective mass of DOS, and m_e is the electron mass [35]. And also, modulation of chemical composition for the TE materials can be alternative method for enhancing the efficiency of TE while at that same time, reduction of the thermal conductivity. For achieving this, moderate doping elements should cause increase the complex electron band structure and lattice phonon scattering. These phonon scattering leads to decrease lattice thermal conductivity. However, in case of electrons, this scattering is negligible due to the higher velocities of carrier. Therefore, modulation of the chemical composition is the primary method for enhancing the TE properties (increasing the

PF and decreasing the thermal conductivity). While, carrier mobility is an external consideration which can affect the *PF*. All of these variations depend on the Mott relation Eq. (6). The reduction of lattice thermal conductivity due to the phonon scattering via the difference between the small mass fluctuation and electronic states is found to increase the TE properties [36].

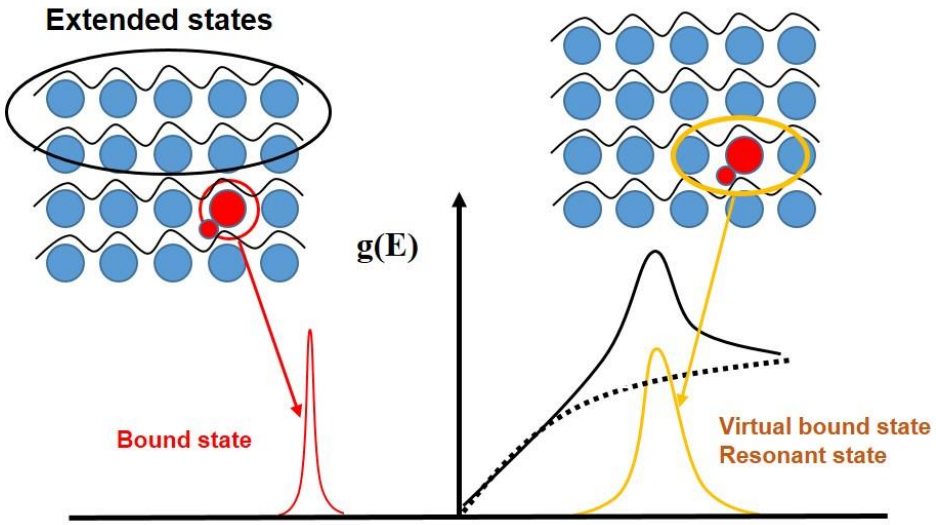

Fig. 1.10. Schematic of the distorted band due to the impurity at the atomic level [34].

For increasing the *PF*, we can use the energy filtering effect. Charge carriers cause the potential barrier in the interface of grain-grain. The charge carrier that crosses the potential barrier shows a strong non-equilibrium energy distribution for high energy charge carriers. Through these phenomena increase the Seebeck coefficient without changing charge carrier concentration as shown in Fig. 1. 11 [37]. Furthermore, electrons of sintered samples are found to scatter across the potential barriers. These potential barriers are formed near the surface of grain boundaries due to the localized states. Thus, these are concerned with dislocation of grain boundary or point defects and also, which can more enhance the *PF* [38].

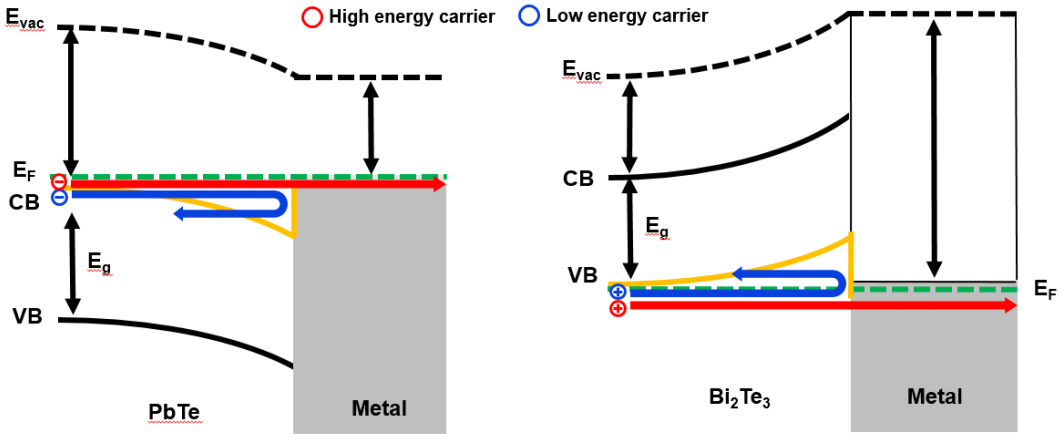

Fig. 1.11. Schematic band diagram of the *n*-type and *p*-type for energy filtering effect [39,40].

1.3.2 Alloying

In a complex bulk TE material, using the alloying materials affect the TE properties of TE efficiency. Through this alloying method, we can achieve the enhancement of the electrical properties for TE materials while reduce the thermal conductivity. Commonly, we can see these effect in most skutterudite compounds as well as in clathrates and Half-heusler TE materials. Especially, the conceptual of PGEC is significant for the skutterudite compounds. The filler elements affect the lattice scattering in a matrix phase of the TE materials, which decrease the lattice thermal conductivity and enhances the *PF* values due to the doping control by filler elements. This phenomenon is called 'rattling effect' and then rattling atom generating disorder of lattice, thus rattling phonon and generating a conducting path for the carrier electron [41, 42]. I want to discuss for skutterudite TE materials in detail later. In most bulk TE materials, the electronic structure is controlled by alloying doping control method. Alloying atoms can cause atomic disorder through the effect of strain field or an induced fluctuation of atom, which decrease the thermal conductivity of lattice part [43, 44].

1.3.3 Nano-inclusion (Nano-structure)

For the bulk TE materials, using the nano-inclusions is reasonable method because it is easy to process and low cost. TE materials with nanocomposite show the high TE properties therefore the use is gradually increasing in TE module, compared with the TE materials with isolated nano-structure or bulk. The composition of spinodal is use to generate a TE materials showing compositional fluctuations at the nanoscale [45, 47]. PbTe-PbS separate the nano-phase

by the growth process, nucleation and spinodal decomposition as shown in Fig. 1.12. For the spinodal decomposition, both compositions of the mixed-phase system share the same lattice, leading to the modulation for spatial of the certain composition at the nano-scale [45]. This modulation for spatial is generated nano-sized particle in the matrix phase, thus making TE materials with nano-structure. Matrix encapsulation makes nano-inclusions within the matrix. During matrix encapsulation, the melted elements are quenched instantly to introduce inclusions at the nano-scale. To improve their crystallinity, the quenched TE materials can be annealed. Nano-scale inclusions can reduce the lattice thermal conductivity due to the scattering of phonon and increase the electrical properties of TE materials [46].

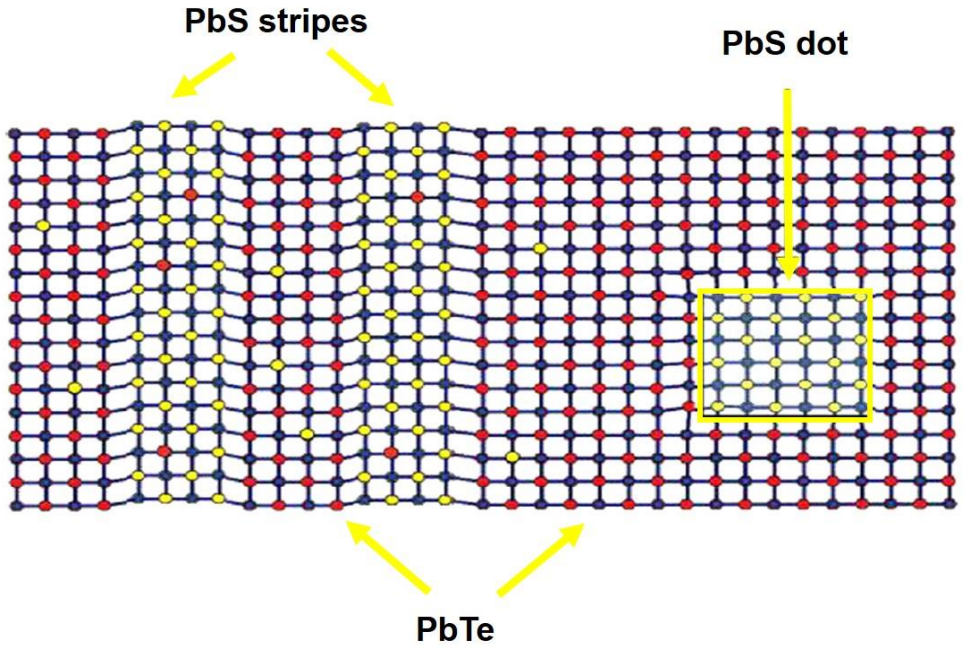

Fig. 1.12. Schematic of stripes (by decomposition) and dot (by nucleation and growth) in (PbTe)/(PbS) [45].

At different length scales, the scattering processes can be affected to alloy scattering at atomic scale, boundary scattering at mesoscale grain, and scattering from nano-scale inclusion as shown in Fig. 1.13. These multi-scale structures of TE materials show higher TE properties than their individual part. When combined together, nano-structuring with a mesoscale grain boundary and alloy doping can enhance the TE properties compared to the nano-structuring effect alone [47].

As I mentioned above, the nanostructuring is an effective method to enhance the TE properties. However, the nanostructured TE materials can be change mechanical properties from the bulk values, which leading to unexpected degrading characteristic. Furthermore, nanostructured materials have a large stored energy in their many grain boundary and thus tend to be unstable. Thus, this can be great obstacle for commercially use of nanostructured TE materials.

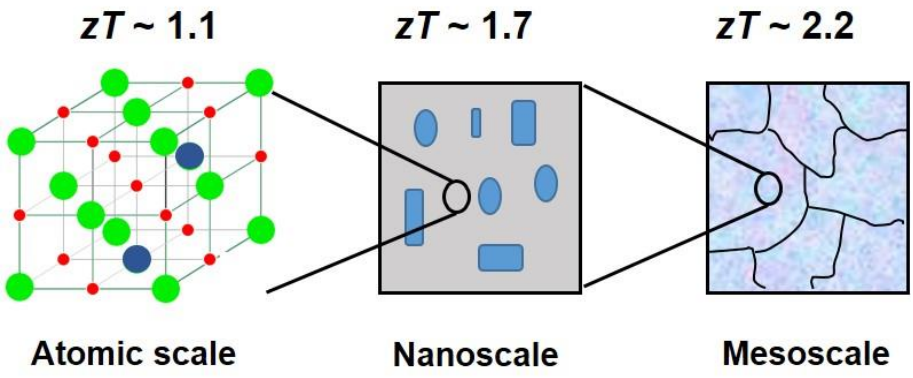

Fig. 1.13. Respective scales for *zT* values [47].

1.4 Skutterudites

The skutterudites derives from a naturally naturally occurring mineral $CoAs_3$, first discovered in Skutterudites, Norway. In general, binary skutterudites is composed of 32 atoms per unit cell, which exhibits the structure of MX_3, where M is the metal element like Ir, Rh, or Co, and X indicates the pnicogen element like As, P, and Sb. As shown in Fig. 1.14, the skutterudite compounds have octahedral structure and two large voids its primitive cell. These voids are large enough to locate the host elements such as metal atoms, thus it is called as filled-skutterudites. The filler atom in void can affect to the lattice phonon-scattering centers, which can decrease the thermal conductivity for lattice part. Introduced elements in the voids cause the significant disorder to the lattice, leading to reduction of lattice thermal conductivity [51].

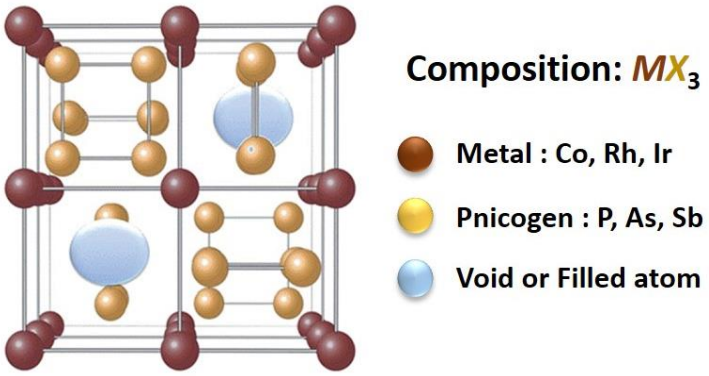

Fig. 1.14. Schematic of the structure of skutterudites [48].

1.4.1 $CoSb_3$-based skutterudites

For $CoSb_3$-based skutterudites, the introduced filler elements in the void sites act as donor, which donate valence electrons to the framework of $CoSb_3$, and then make the heavily doped TE materials as semiconductor. In $CoSb_3$-based skutterudites have 18 valence electrons per primitive cell, nine of which are share by Co and three are shared by each Sb atom. Thus, $CoSb_3$-based skutterudites have a complex phase with exhibiting semiconducting, and also, these are stable at the high temperature up to around 1150 K. Furthermore, $CoSb_3$-based skutterudites can use high-temperature TE applications. Also, it has an narrow bandgap about ~ 0.6 eV. In case of Co-rich skutterudites are used *n*-type TE materials, on the other hand, in case of Sb-rich skutterudites are used *p*-type TE materials. These compounds can be changed by substituting filler elements in place of Sb and Co sites, such as substituting the Sb sites with Te or Sn and the Co sites with Ni or Fe. As shown in Fig. 1.15, the substituted elements act as dopants by accepting or donating electrons [49]. In table 1.2, I summarize the properties of some atoms used as substitution elements in $CoSb_3$-based skutterudites [52].

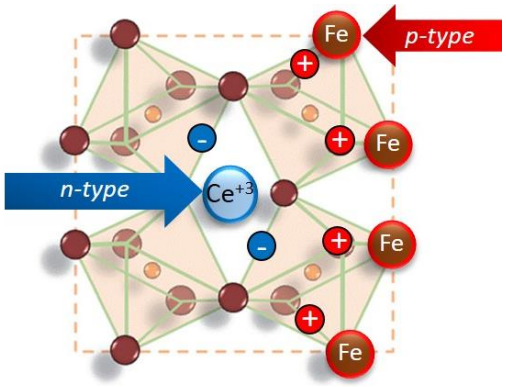

Fig. 1.15. How to make the *n*-type and *p*-type skutterudites [49].

1.4.2 Filled-skutterudites

The $CoSb_3$-based skutterudite shows high *PF* values about 6 μV/cmK compared with other TE materials. While skutterudite compounds have higher thermal properties about 10 W/mK at room temperature. At 600 K, $CoSb_3$-based skutterudite exhibits thermal conductivity values about 5 W/mK, however, this thermal conductivity value is lower compared with Te-based TE materilas, such as Bi_2Te_3 or PbTe [53]. Thus, the $CoSb_3$-based skutterudite exhibits the lower *zT* values due to their higher thermal conductivity value. As I mentioned before, to overcome this problem, we can use the rattling effect by fluctuation of filler atom, which affect the lattice phonon scattering. There are many studies for filled-skutterudites TE materials [54-56]. In case of $Yb_xCo_4Sb_{12}$ system shows the *zT* values of ~ 0.3 and ~ 1 at room temperature and 600 K, respectively. For Yb-filled $CoSb_3$ based-skutterudite, the *zT* is enhanced from 7 to 10 due to the filler elements (Yb), compared with un-doped ones. This phenomenon is called as 'rattling effect', which can observe in TE materials of PGEC concept decrease the thermal conductivity for lattice part without reduction of electrical properties [55]. Recently, many studies have investigated that a reduction due to the nano-structuring or grain size control can increase the TE properties of $CoSb_3$-based skutterudite [56]. In Table 1.3, I summarize the effect of filler elements for the TE properties at various temperature.

Table. 1.2. Thermoelectric and physical properties of various atoms used in the $CoSb_3$ [52].

Element	S (μV/K)	σ (S/cm)	κ (W/mK)	M.P. (°C)	Structure	Atomic radius
Co	-31	0.17	100	1495	HCP	1.7
Sb	47	0.03	24	631	R.H.	1.5
Yb	30	0.04	35	824	FCC	2.4
Ca	10	0.30	201	839	FCC	2.2
Ba	12	0.03	18	729	BCC	2.8
Ce	6	0.01	11	798	FCC	2.7

Table. 1.3. Thermoelectric properties of various $CoSb_3$ based skutterudites [55,56].

Material	*S* (μV/K)	*σ* (S/cm)	*PF* (μW/cmK)	*κ* (W/mK)	*zT* at 327 °C
$In_{0.2}Ce_{0.1}Co_4Sb_{12}$	340	230	26.6	1	1.6
$In_{0.25}Ce_{0.2}Co_4Sb_{12}$	300	450	40.5	1.6	1.5
$In_{0.2}Ce_{0.1}Yb_{0.1}Co_4Sb_{12}$	325	320	33.8	1.7	1.2
$In_{0.2}Ce_{0.1}Sm_{0.1}Co_4Sb_{12}$	305	280	26	1.2	1.3
Co_3FeSb_{12}	110	-	0.2	0.9	0.2
$CaFe_3CoSb_{12}$	150	160	25.2	2.5	0.6

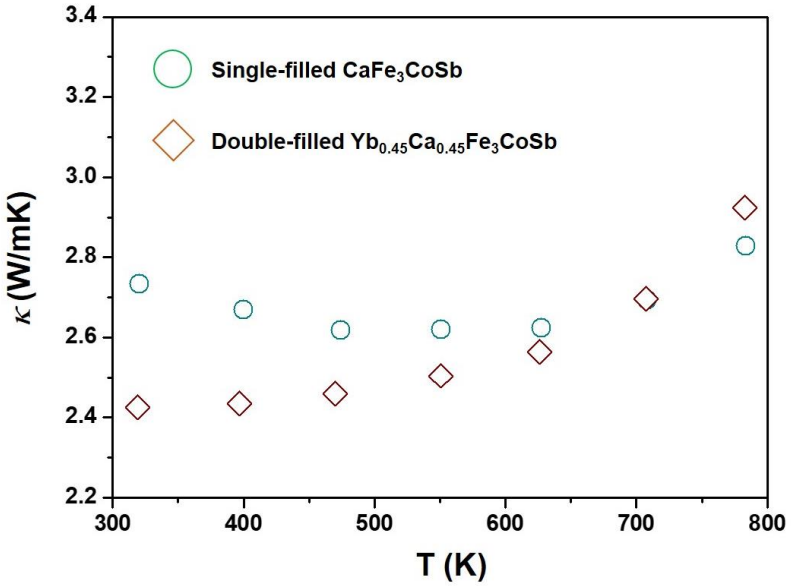

Fig. 1.16. Thermal conductivity of Single-filled $CeFe_3CoSb_{12}$ and double filled $Yb_{0.45}Ca_{0.45}Fe_3CoSb_{12}$ [56].

1.5 Purpose of Present Study

In order to solve environmental pollution and energy crisis caused by increased energy consumption due to industrialization and urbanization, many countries and companies are focusing on development of eco-friendly energy such as renewable energy thermoelectric (TE) materials and solar cells. Among them, thermoelectric generation (TEG) technology is an environmentally friendly power generation technology that does not cause any pollution and is less toxic than other generation technology, thus it is expected as a promising technology that can supplement low energy efficiency of fossil fuel because it uses waste heat. In addition, as nano-technology and manufacturing process technologies develop, efficiency of TE materials is increasing, and many researchers are investigating them for practical application. However, although high TE efficiency is possible by using nano-technology, it is difficult to commercialize bulk TE materials due to the limits of nano-technology. Although the development of manufacturing technology also shows high thermal conversion efficiency, the efficiency of *p*-type bulk TE materials, which is lower TE performance than *n*-type materials, thus, it is difficult to commercialize.

Therefore, in this study, the objective is to improve the TE performance of skutterudite as *p*-type bulk TE material for commercial use. Skutterudite has two void in its basic structure, so it

can be filled various elements. Furthermore, filled elements can vibrate due to the weak coupling of elements in the void, which can lead to reduce thermal conductivity. The elements in the void also act as a donor, at the same time, which can adjust the carrier density. In general, to synthesize *p*-type skutterudite, Co is substituted by another element, in this study, Fe is substituted with a Co to synthesize *p*-type skutterudite. And also, the substituted Fe was expected to reduce the thermal conductivity by point defect.

In Chapter III, we synthesized In filled *p*-type skutterudite compounds. And then, we investigated filling fraction of In and their effects for TE performance. And also, we confirmed the optimal composition of In contents to obtain the maximum TE performance. Additionally, we considered about the effect of nano-sized impurities (such as InSb) generated during the synthesis process for TE performance.

In Chapter IV, we selected Ce as filler because Ce-filled skutterudits show low thermal conductivity and high TE properties. Furthermore, we substituted different amounts of Fe, the effect of these changes on TE properties was investigated. And we optimize the carrier concentration by adjusting the Ce/Fe ratio.

In Chapter V, we synthesized Ga co filled *p*-type skutterudites based on the optimal conditions in Chapter IV to improve the TE performance. In particular, we investigated Ga behavior because it could be located in both the void site and the Sb site. And also, we investigated the effect of double-filming on thermal conductivity and optimized chemical composition to improve TE performance.

As a results, in this study, in order to improve the TE performance of bulk *p*-type TE materials, various elements (In, Ce, Ga) were inserted into the $CoSb_3$-based skutterudite with high TE performance and excellent mechanical properties in the intermediate temperature range and investigate their behavior and effect on TE properties. Furthermore, we attempted to improve the electrical properties by optimizing the carrier concentration using the optimization of chemical composition (Fe substitution ratio).

1.6 References

[1] US DOE EIA *Ann. Energy Rev.* (2012).

[2] C. Gayner, K. Kar *Prog. Mater. Sci.* **83**, 330 (2016).

[3] W. Liu, J. Hu, Y. Liu, et al., *Mater. Today Phys.* **1**, 50 (2017).

[4] G. Snyder, E. Toberer *Nat. Mater.* **7**, 105 (2008).

[5] H. Goldsmid, Springer Berlin Heidelberg, Berlin, Heiderberg. (2010).

[6] A. Ioffe, Semiconductor thermoelements, and Thermoelectric cooling, Infosearch London (1957).

[7] I. BI, A. WH. *Rec. Pat. Elect. Eng.* **2**, 27 (2009).

[8] R. Makala, K. Hagannadham, B. Scales et al., *J. Appl. Phys.* **94**, 3907 (2003).

[9] E. Quarez, K. Hsu, et. al., *J. Am. Chem. Soc.* **127**, 9177 (2005).

[10] T. Herman, P. Yaylor, et. al., *J. Electron Mater.* **40**, 635 (2011)

[11] F. Rosi *Solid State Electron* **11**, 833 (1968).

[12] Y. Pei, Y. Liu. *J. Alloy Compd.* **514**, 40 (2012)

[13] S. Ur, P. Nash, R. Schwarz, et. al., *Met. Mater. Int.* **11**, 435 (2005)

[14] C. Recknagel, N. Reinfried, et. al., *Sci. Technol. Adv. Mater.* **8**, 357 (2007)

[15] R. Schmidt, E. Case, et. al., *J. Electron. Mater.* **41** 1210 (2012)

[16] R. Hummel Electronic properties of materials 3rd ed. New York, Springer (2001).

[20] L. Hu, T. Zhu, et al., *Adv. Funct. Mater.* **24**, 5211 (2014).

[21] L. Zhao, B. Zhang, et al. *J. Alloy compd.* **455**, 259 (2008).

[22] L. Zhao, J. He, et al., *J. Am. Chem. Soc.* **134**, 7902 (2012).

[23] K. Biswas, J. He, C. Wu, et al., *Nature* **489**, 414 (2012).

[24] Y. Gelbstein, Z. Dashevsky, et. al., *Phys. Rev. B* **363**, 196 (2005).

[25] A. Dmitriev, I. Zvyagin, et. al., *Phys. Usp.* **53**, 189 (2010).

[26] J. Li, S. Li, Q. Wang, L. Wang, et. al., *J. Electron Mater.* **40**, 2063 (2011).

[26] D. Parker, D. Singh *Phys. Rev. B* **8**, 035204 (2010).

[27] M. Zebarjadi, G. Joshi, et. al., *Nano Lett.* **11**, 2225 (2011).

[28] B. Liao, M. Zebarjadi, K. Esfarjani, et. al., *Adv. Mater.* **25** 1577 (2012).

[29] B. Liao, M. Zebarjadi, G. Chen, et. al., *Phys. Rev. Lett.* **109**, 126806 (2012).

[30] J. Friedel *J. Phys.* **34**, 1190 (1956).

[31] G. Mahan, *J. Appl. Phys.* **65**, 1578 (1989).

[32] D. Bilc, S. Mahanti, M. Kanatzidis *Phys. Rev. B* **74**, 125202 (2006).

[33] Y. Zhao, X. Liao, J. Hong *Mater. Chem. Phys.* **87**, 149 (2004).

[34] A. Hmood, A. Kadhim, et. al., *Superlat. Microsturct.* **51**, 825 (2012).

[35] Y. Pei, X. Shi, A. Lalonde, et. al., *Nature* **473**, 66 (2011).

[36] G. Zhu, H. Lee, Y. Lan, et. al., *Phys. Rev. Lett.* **102**, 196803 (2009).

[37] B. Wolfing, C. Kloc, et. al., *Phys. Rev. Lett.* **86**, 4350 (2001).
[38] D. Narducci, E. Selezneva, et. al., *J. Solid State Chem.* **193**, 19 (2012).
[39] S. Faleev and F. Leonard *Phys. Rev. B* **77**, 214304 (2008).
[40] D. Ko, Y. Kang, and C. Murray, *Nano Lett.* **11**, 2841-2844 (2011).
[41] J. Leszczynski, K. Wojeciechowski, et. al., *J. Therm. Anal. Calorim.* **105**, 211 (2011).
[42] W. Liu, B. Zhang, J. Li, L. Zhao *J. Appl. Phys.* **40**, 6784 (2007)
[43] G. Nolas, M. Kaeser, R. Littleton, et. al., *Appl. Phys. Lett.* **77**, 1855 (2000).
[44] J. Yang, H. Li. et. al., *Adv. Funct. Mater.* **18**, 2880 (2008).
[45] Q. Shen, L. Chen, et. al., *Appl. Phys. Lett.* **79**, 4165 (2001).
[46] W. Liu, X. Yan, G. Chen, Z. Ren *Nano Energy* **1**, 42 (2012).
[47] K. Biswas, J. He, I Blum, et. al., *Nature* **489**, 414 (2012).
[48] M. Rull-Bravo et. al. *RCS Adv*. **5**, 41653 (2015).
[49] D. Thompson et. al. *Acta Mater.* **92**, 152 (2015).
[50] G. Nolas, D. Morel, et. al., *Ann. Rev. Mater. Sci.* **29**, 87 (1999).
[51] J. Sootsman, D. Chung, et. al., *Angew. Chem. Int. Ed.* **48**, 8616 (2008).
[52] M. Dresselhaus, G. Chen, et. al., *Adv. Mater.* **19**, 1043 (2007).
[53] S. Ballikaya, G. Wang, et. al., *J. Electron Mater.* **40**, 570 (2011).
[54] J. Graff, S. Zhu, T. Holgate, et. al., *J. Electron Mater.* **40**, 696 (2011).
[55] X. Shi, H. Kong, et. al., *J. Phys. Lett.* **92**, 182101 (2008).
[56] D. Thompson et. al., *Acta Mater.* **92**, 152 (2015).

CHAPTER II

Experimental Methods

2.1 Sample Preparation

In this thesis, we prepared the polycrystalline bulk TE materials by using a traditional solid-state reaction and spark plasma sintering (SPS). To analysis the polycrystalline structure of bulk the samples, we characterized by X-ray diffraction (XRD, Ultima IV). For lattice parameters of bulk samples, we use the standard silicon and PDXL. The microstructure and elemental distribution of the bulk samples were investigated by using a field emission scanning electron microscopy (FE-SEM; JSM-6500F), which equipped an energy dispersive X-ray spectroscopy (EDS). In case of electrical resistivity and Seebeck coefficient of samples, we could measure using ZEM-3. Charge carrier concentration (n_H) and carrier mobility (μ_H) were measured by Hall effect measurement. Thermal conductivity (κ) could obtain heat capacity (C_p), from thermal diffusivity (α), and sample density (d) based on the $\kappa = \alpha C_p d$. C_p, which was estimated from the Dulong–Petit model, $C_p = 3nR$, in where n is the atoms number and R is the ideal gas constant. Thermal diffusivity (α) could be obtained by the laser flash method in vacuum condition using available apparatus (NETZSCH, LFA467).

2.1.1 Solid State Reaction

The solid-state reaction is using for the preparation of crystal solids from solid starting materials which is very effective method. At room temperature, solids never react together naturalistically and it is need to heat much higher temperatures, often to 900 to 1600 °C for the reaction of our materials. The solid state reaction depend on the various factors such as reaction conditions, surface area of the solids, structural properties of the reactants, the free energy change associated with the reaction and their reactivity etc. [1].

2.1.2 Spark Plasma Sintering

Various sintering techniques have been investigated for high densification with a desired phase composition and microstructure. Spark plasma sintering (SPS) process is effective for high heating rate with minimal grain growth [2]. A schematic of the method is shown in Fig. 2.1. The mechanism of the spark plasma sintering is based on the micro spark discharge in the gap between

individual particles in compact powders. The spark plasma sintering proceeds through a three-stage process. In first stage, the surface of particle melt and fuse to each other forming “necks” between neighboring powder particles. In second stage, the joule heat, generated by pulsed DC electrical current, reacts between the necks connecting individual particles. The diffusion of the atoms in the necks was increased and enhanced their growth by joule heat. In third stage, the heated samples become softer and exerts plastic deformation under the uniaxial force, leading to the high densification of the powder compact of its theoretical density.

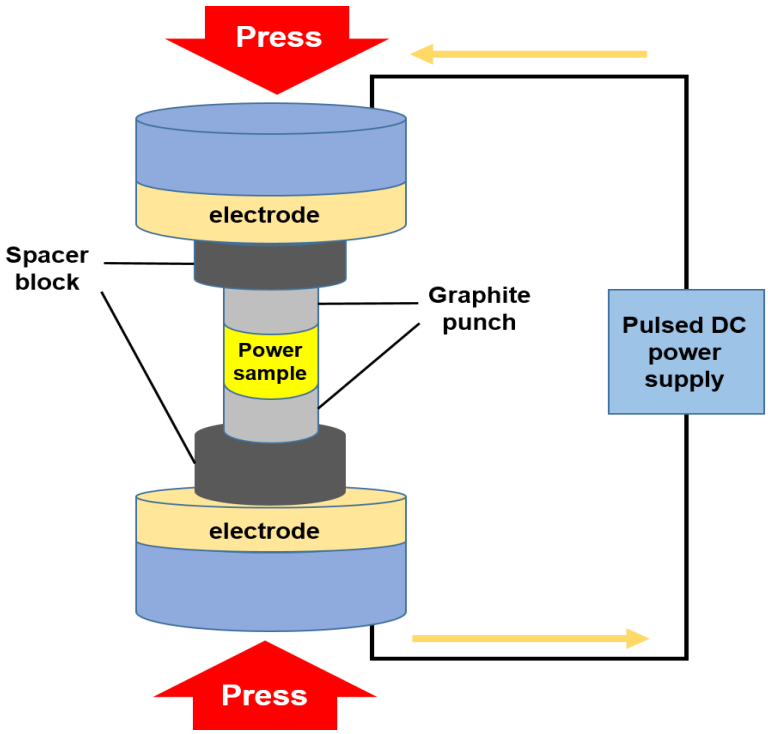

Fig. 2.1. Schematic of spark plasma sintering technique.

2.1.3 X-ray Powder Diffraction

In general, we can obtain the informations of the phase compositions and crystal structures from X-ray diffraction (XRD) (ULTIMA IV, Rigaku), which using Cu-Kα radiation ($\lambda = 1.5406$ Å) with a scintillation or semiconductor detector. The lattice parameter, theoretical density, and thermal expansion coefficient were determined by the XRD results. The materials consisted of regular arrays of atoms can be confirmed by using a data of X-ray diffraction patterns because crystalline materials have unique diffraction patterns. Since X-ray is electromagnetic radiation

waves, which is scattered by atoms. X-ray smashing an electron and then produces secondary waves. In here, because X-ray energy is much greater than that of a valence electron energy, thus this phenomenon can occur. This elastic scattering can be modeled using the Thomson scattering, which is the interaction of an electromagnetic ray for the free electron. Thus, the intensity of scattering can be expressed as [3]:

$$I_e = I_0 \left(\frac{e^4}{m^2 c^4 r^2}\right) \frac{1+cos^2 2\theta}{2} \quad (2.1)$$

where m is the electron mass, I_0 represents the intensity of the X-ray beam, r is the distance to observed position, c is the light speed, and e is the charge of electron.

The incident waves have wavelengths comparable to the spacing between atoms. Fig. 2.2 shows geometry for interference of a wave scattered from two planes separated by an inter-planar spacing. From Fig. 2.2. Angle of incidence of the two parallel rays is considered as θ. The inter-planar spacing, d, is the difference in path for the X-ray scattered from the top plane and bottom plane. When the difference in path length for the top and bottom X-ray is equal to one wavelength, λ, the constructive wave interference was occurred by Bragg's law:

$$n\lambda = 2dsin\theta \quad (2.2)$$

where n is any integer. These specific directions appear as spots on the diffraction pattern, which called reflections. A reflection from a crystalline material contains many distinct peaks, corresponding to a different interplanar spacing. And they are to be indexed the records of Miller index of each reflection, (hkl).

A powder X-ray diffractometer consists of the X-ray tube, the sample stage, and the detector. The incident angle is defined between the X-ray beam source and the sample. The diffraction angle, 2θ, is defined between the incident beam and the detector. The incident angle is always one half of the detector angle 2θ.

2.1.4 Microstructure and Morphology

In general, the surface microstructures and morphology of the obtained samples were characterized by FE-SEM and EDX analysis. In a typical, FE-SEM multiple condenser lenses and electron gun produce an electron beam, the rays at a variety of angles are diverted by electromagnetic scan coils (first set). The second set of scan coils diverts the beam back across the optic axis. All the generated rays pass through the final aperture lens and strike the specimen surface at various points. The resultant signals contain low energy secondary, backscattered electrons and

high energy back scattered electrons, X-rays, and visible, luminescent radiation in the UV, and infrared. SEM and EDS are obtained by a scanning electron image (SEI) detector, and an EDS detector, respectively. Fig. 2.3 represents the schematic of SEM.

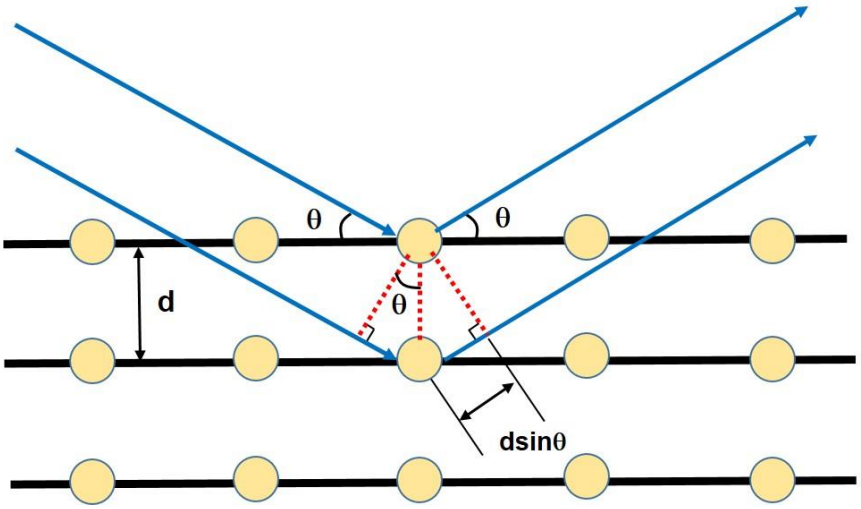

Fig. 2.2. Schematic illustration of powder X-ray diffraction.

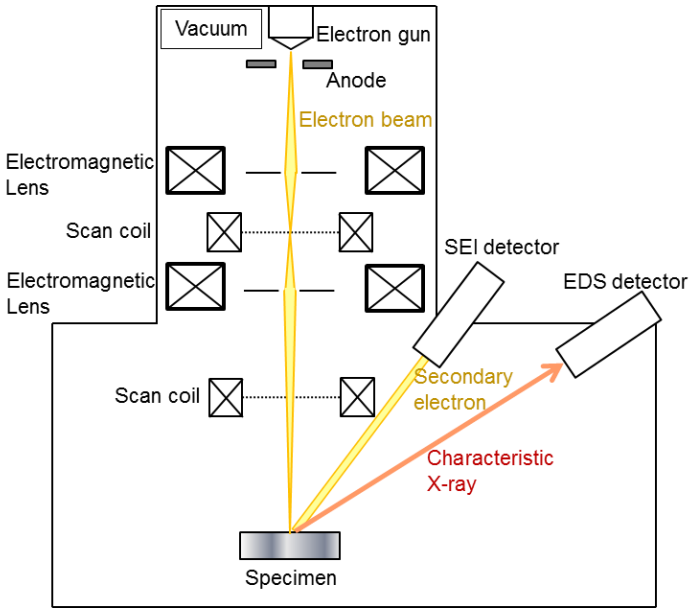

Fig. 2.3. Schematic illustration of FE-SEM.

2.1.5 Seebeck Coefficient and Resistivity

At high temperature, the thermopower and resistivity of the samples were investigated by using the ZEM-3 (ULVAC) under helium atmosphere condition as shown in Fig. 2.4. The electrical resistivity was obtained by the four probe method. Two thermocouples are attached to the sample to measure the voltage across A and B as ΔV. At the meantime, the temperature is measured between two thermocouples as T_H and T_L. In this way, the measuring temperature T would be

$$T = \frac{(T_H + T_L)}{2} \tag{2.3}$$

The Seebeck coefficients (S) is obtained by the following equation:

$$S = \frac{\Delta V}{\Delta T} \tag{2.4}$$

ΔV is the Seebeck voltage generated between two thermocouples on surface of the sample, across the direction of the temperature gradient. T_H (near the hot side) and T_L (near the cold side) are represent absolute temperatures at the two points. In general, the measurement was performed by applying three temperature gradients of ΔT = 20, 30, and 40 K between two blocks at each temperature T, we use the average value of three data as the experimental value.

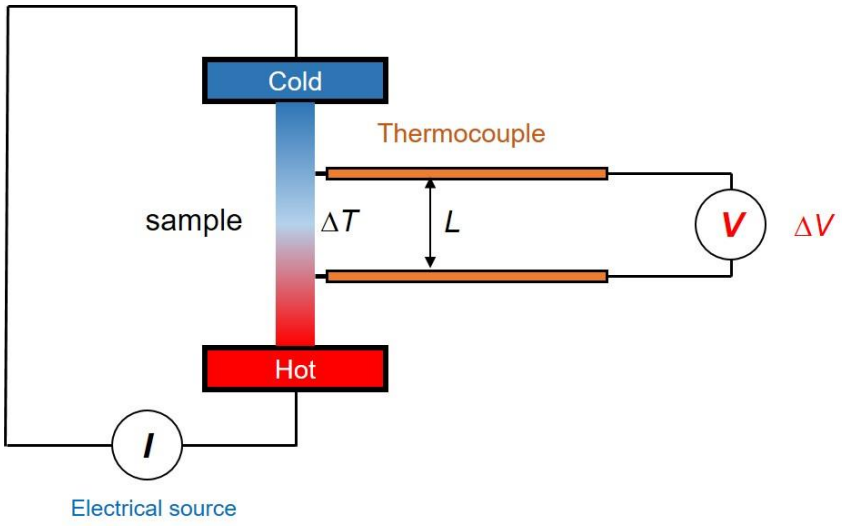

Fig. 2.4. Schematic illustration of ZEM-3 measurement.

2.1.6 Thermal Conductivity

The thermal conductivity (κ) was obtained from the thermal diffusivity (d) specific heat capacity at constant pressure (C_p), and density as following equation:

$$\kappa = dC_p\rho \tag{2.5}$$

The thermal diffusivities were determined by a laser flash method using an LFA457 instrument. The laser flash method is illustrated as shown in Fig. 2.5. Prior to thermal diffusivity measurement, both faces of samples were coated by graphite using graphite spray to improve the laser absorption at the lower surface and to increase the intensity of the emissions of the upper surface. The theory of the method for thermal diffusivity is followed [4]:

If the distribution of initial temperature within a thermally insulated uniform thickness (h_k) of sample is T (x,0), the distribution of temperature at later time t is given by:

$$T(x,t) = \frac{1}{h_k}\int_0^{h_k} T(x,0)\,dx + \frac{2}{h_k}\sum_{n=1}^{\infty} exp\left(\frac{-n^2\pi^2 td}{{h_k}^2}\right) \times \cos\frac{n\pi x}{h_k}\int_0^{h_k} T(x,0)\cos\frac{n\pi x}{h_k}\,dx \tag{2.6}$$

If a radiant energy pulse (Q) is simultaneously and uniformly absorbed in the shallow depth g at the lower surface $x = 0$ of a thermally insulated material of uniform thickness (h_k) the distribution of temperature at that instant is expressed by:

$$T(x,0) = \frac{Q}{\rho C_p g} \quad (0 < x < g) \tag{2.7}$$

and

$$T(x,0) = 0 \quad (g < x < h_k) \tag{2.8}$$

Under the initial condition, Eq. (2.8) can be written by

$$T(x,t) = \frac{Q}{\rho C_p h_k}\left[1 + 2\sum_{n=1}^{\infty}\cos\frac{n\pi x}{h_k}\frac{\sin(n\pi g/h_k)}{(n\pi g/h_k)} \times exp\left(\frac{-n^2\pi^2}{{h_k}^2}td\right)\right] \tag{2.9}$$

It follows $\sin(n\pi g/h_k) \approx (n\pi g/h_k)$ because g is a quite small for opaque materials. At the upper surface where $x = h_k$, the temperature can be expressed as

$$T(h_k,t) = \frac{Q}{\rho C_p h_k}\left[1 + 2\sum_{n=1}^{\infty}(-1)^n exp\left(\frac{-n^2\pi^2}{{h_k}^2}td\right)\right] \tag{2.10}$$

Dimensionless terms, V and ω can be defined as

$$V(h_k,t) = \frac{T(h_k,t)}{T_M} \tag{2.11}$$

and

$$\omega = \frac{\pi^2 td}{{h_k}^2} \tag{2.12}$$

In here, T_M is the maximum temperature at the upper surface. The combination of Eq. (2.10), (2.11), and (2.12) produces

$$V = 1 + 2\sum_{n=1}^{\infty}(-1)^n exp(-n^2\omega) \tag{2.13}$$

The produced Eq. (2.13) is plotted as shown in Fig. 2.5. From Eq. (2.13) and Fig. 2.5, h_k have been deduced. When V is equal to 0.5, ω is equal to 1.38 as follows:

$$d = \frac{1.38{h_k}^2}{\pi^2 t_{1/2}} \tag{2.14}$$

where $t_{1/2}$ is the initiation of the pulse laser until the temperature rise of the upper face of the sample reaches to the half-maximum. The uncertainty for the thermal diffusivity measurements can be expressed by

$$d + \Delta d = \frac{1.38(h_k + \Delta h_k)^2}{\pi^2 (t_{1/2} + \Delta t)} \tag{2.15}$$

where Δd, Δt, and Δh_k are uncertainty of d, $t_{1/2}$, and h_k, respectively. When the surface of the sample is covered by a carbon film, additional time is needed to reach heat from the lower to upper surface of the sample due to the thermal resistance of the carbon film. Thus, the variation in the thickness of the carbon is associated with Δt. Δh_k is associated with the variation in h_k or uncertainty in the measurements of h_k. Although the quantitative estimation of Δd must be done by error propagation law using Δt and Δh_k, Eq. (2.15) allows qualitative discussion about Δd. Eq. (2.15) shows that assuming Δt and Δh_k to be constant, Δd becomes small with increasing $t_{1/2}$. The value of $t_{1/2}$ becomes larger when a material has lower thermal conductivity, which indicates that the uncertainty in the thermal diffusivity measurements become small when the sample has very low thermal conductivity.

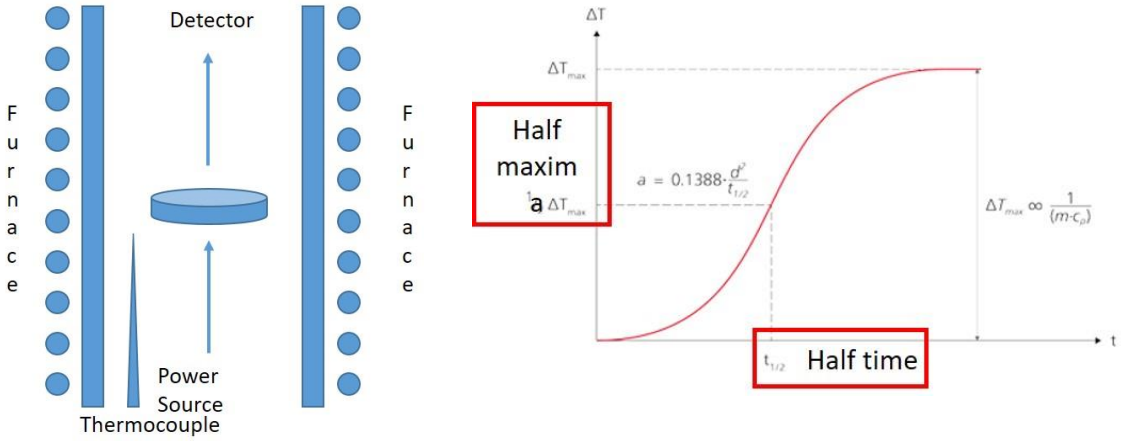

Fig. 2.5. (a) Schematic illustration for the laser flash and (b) Upper surface temperature history.

2.1.7 Carrier Concentration and Mobility

The Hall coefficient (R_H) was performed by the Van der Pauw method using Resitest 8300 (Toyo Co. Ltd.) apparatus at room temperature under an applied magnetic field of 0.5 T. We can obtain the values of the Hall carrier concentration (n_H) and Hall mobility (μ_H) from the measured Hall factor (R_H) assuming a single band model and Hall factor of 1 with following equations [5]:

$$n_{\mathrm{H}} = \frac{\gamma_{\mathrm{H}}}{eR_{\mathrm{H}}} \quad \text{and} \quad \mu_{\mathrm{H}} = \frac{R_{\mathrm{H}}}{\rho} \tag{2.16}$$

In here, R_H and ρ represent the Hall coefficient and the electrical resistivity, respectively, and γ_H is the Hall factor which is given by as following equations:

$$\gamma_{\mathrm{H}} = \frac{3\sqrt{\pi}}{4} \frac{(2s+3/2)\,!}{[(s+3/2)\,!]^2} \tag{2.17}$$

The Hall coefficient is given by the following equation using the magnetic field B, Hall voltage V, the current I, and the sample's thickness δ.

$$R_{\mathrm{H}} = \frac{|V_{23}|\delta}{I_{14}B} = \frac{\delta}{B} R_{12,34} \tag{2.18}$$

Here, twice measurements give two resistances:

$$R_{12,34} = \frac{|V_{23}|}{I_{14}} \quad \text{and} \quad R_{23,41} = \frac{|V_{41}|}{I_{23}} \tag{2.19}$$

The numbers indicate proves shown in Figure 2.6. Then, the resistivity is calculated from

$$\rho = \frac{\pi}{\ln 2} \delta \frac{R_{12,34} + R_{23,41}}{2} f \tag{2.20}$$

The factor f depends on the ratio $R_{12,34}/R_{23,41}$ as shown in Figure. 2.6.

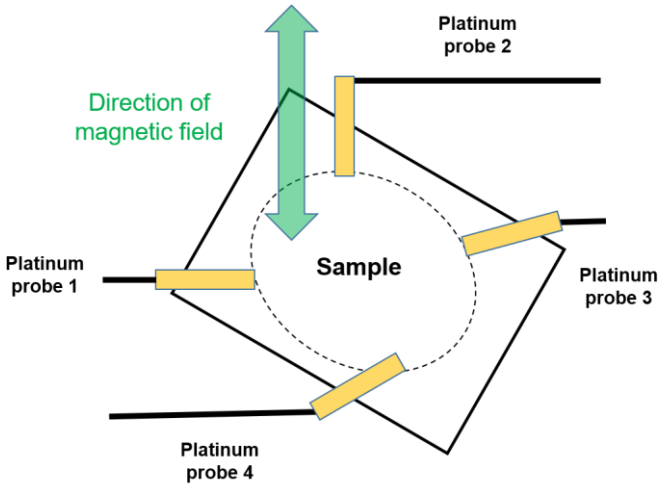

Fig. 2.6. Schematic illustration of van der Pauw's method.

2.2 References

[1] J. Gilfrich, *X-Ray Spectrom.* **22** (1993).

[2] H. Inaba and T. Yamamoto, *Thermal measurement* **10**, 132 (1983).

[3] D. M. Rowe, *CRC Handbook of Thermoelectrics* (Boca Raton, FL, CRC Press, 1995).

[4] G. A. Slack, *J. Solid State Phys.* **34**, 151 (1979).

[5] L. J. v. d. Pauw, *Philips Tech. Rev.* **20**, 220 (1958).

CHAPTER III

Thermoelectric Properties of In Single-Filled *p*-type Skutterudites

Although Indium (In)-filled $CoSb_3$ skutterudites are good *n*-type thermoelectric (TE) material, the In-filled *p*-type skutterudites have been scarcely studied. For TE devices, both *p*- and *n*-type materials with similar characteristics are simultaneously required. Based on the simple electron counting, it is expected that substitution of Fe for Co in $CoSb_3$ leads to *p*-type doping. Here, we have attempted to realize *p*-type characteristics in In-filled $(Fe,Co)Sb_3$. Polycrystalline samples with nominal compositions $In_xFeCo_3Sb_{12}$ (x = 0.3, 0.5, 0.7, and 0.9) were prepared and their phase state, microstructure, and high-temperature TE properties were examined. All samples showed positive Seebeck coefficient values, i.e., *p*-type characteristics. We confirmed that the filling fraction limit was between x = 0.5 and 0.7 in $In_xFeCo_3Sb_{12}$, and the x = 0.5 sample exhibited the best TE properties. The maximum value of the dimensionless figure of merit zT was 0.39 at 705 K.

3.1 Introduction

In this study, therefore, we set the sample compositions as $In_xFeCo_3Sb_{12}$ (x = 0.3, 0.5, 0.7, and 0.9) and investigated the phase state as well as the TE properties. Polycrystalline samples of $In_xFeCo_3Sb_{12}$ (x = 0.3, 0.5, 0.7, and 0.9) in the nominal compositions were prepared. The criteria for nominal composition are making p-type and single-phase TE materials. Among the In-filled samples, single-phase samples could be obtained only in the composition of Fe:Co = 1:3. And then, I confirmed TE properties (S, σ, and κ) through the examination from room temperature to 773 K. Effects of the In-filling and the Fe substitution on the TE properties were investigated.

3.2 Results and Discussion

Figure 3.1 shows the powder XRD patterns of the polycrystalline samples with nominal compositions $In_xFeCo_3Sb_{12}$ (x = 0.3, 0.5, 0.7, and 0.9). The peaks of the major phase in all samples were indexed to the skutterudite phase. In addition to the skutterudite peaks, a few peaks of the $(Fe,Co)Sb_2$ phase, a solid solution of $FeSb_2$ and $CoSb_2$, were observed. The impurity peaks were negligible in the samples with x = 0.3 and 0.5, while the peak intensity increased with increasing x.

As summarized in Table 3.1, the lattice parameters for the skutterudite phase slightly increased with increasing x up to $x = 0.7$ and then remained nearly constant, indicating that the filling fraction limit of In in $In_xFeCo_3Sb_{12}$ would be between $x = 0.5$ and 0.7. Furthermore, the lattice parameters of all samples were larger than not only the maximum (~ 0.9058 nm) of In-filled $CoSb_3$ reported by Tang et al. [17] but also the maximum (~ 0.90447 nm) of $In_zCo_{4-x}Fe_xSb_{12}$ ($z = 0.05$, 0.25; $x =$ 0.5, 1.0, 1.5) reported by Park et al. [22] All samples had enough high bulk densities (estimated as over 98 % of the theoretical density) for TE characterizations.

Figure 3.2 shows the FE-SEM images of the samples with nominal compositions $In_xFeCo_3Sb_{12}$ ($x = 0.3$, 0.5, 0.7, and 0.9). All samples were dense with no remarkable cracks or pores. The samples with $x = 0.3$ and 0.5 had even smaller and more uniform grains (0.5 ~ 1 μm) than those of the other samples. The results on the grain size let us consider that the void site filling by In encourages the grain growth. The small and uniform grains would be effective for scattering of heat carrying phonons. As shown in Figs. 3.2(f) and 3.2(h), in the samples with $x = 0.7$ and 0.9, the nanoparticles with the size below 100 nm were clearly observed at the grain boundaries. The chemical composition of the nanoparticles couldn't be clearly determined since the resolution of EDS analysis was too low to perform the quantitative analysis for the nanoparticles. Note that here, however, the previous works have confirmed that In exceeded the filling limit reacted with Sb and formed the InSb nanoparticles [23,24]. Table 3.2 shows the chemical compositions of the skutterudite phase determined by the quantitative EDS analysis. The data shown here are the average values of the point analyses performed for more than 20 different grains. These data are within the standard deviation range (± 3 %). However, it is possible to perform a more precise analysis through the other methods such as TEM-EDS, ICP-AP and ICP-MS. The In content in the skutterudite phase increased up to $x = 0.7$ with increasing x and then decreased at $x = 0.9$, while the Fe/Co ratio values of all samples were nearly constant (0.25 ± 0.02). This result indicates that the filling fraction limit of In would be between $x = 0.5$ and 0.7, which is well consistent with the XRD results. Despite of the low In actual content (~ 0.19), the sample with $x = 0.3$ had the large lattice parameter compared to an In-filled $CoSb_3$, which is due to the substitution of Fe for Co. Moreover, the actual contents of In (≥ 0.29) in the skutterudite phase of the samples with $x \geq 0.5$ were definitely larger than the solubility limit (0.27 ± 0.01) of In in Co_4Sb_{12} [17]. The results indicate that the substitution of Fe for Co increases the lattice parameter, which leads to the additional incorporation of In into the skutterudite phase.

Room temperature values of the ρ, R_H, n_H, and μ_H are summarized in Table 3.3. The R_H

values of all samples were positive, i.e., *p*-type conduction, which is consistent with the sign of the S as shown in Fig. 3.3(b). The n_H decreases as adding In, which would be due to the typical behavior in the *p*-type filled skutterudites where the excess holes generated from the substitution of Fe for Co could be compensated by the electrons donated by fillers [13]. On the other hand, the μ_H increased as adding In, which would be caused by the decrease in the carrier-carrier scattering effect.

Figures 3.3(a), 3.3(b), and 3.3(c) show the temperature dependences of the *S*, electrical resistivityρ (= σ^{-1}), and power factor $S^2\rho^{-1}$ (= $S^2\sigma$), respectively, for polycrystalline samples with nominal compositions $In_xFeCo_3Sb_{12}$ (x = 0.3, 0.5, 0.7, and 0.9) and $In_{0.25}Fe_{1.5}Co_{2.5}Sb_{12}$ [22] for comparison. The ρ of all samples increased with temperature, indicating metallic behavior. The ρ, moreover, increased with increasing the nominal In content over the entire temperature range, which would mainly attribute to the decrease of carrier concentration (n_H) as listed in Table 3. The *S* values of all samples nearly increased up to around 700 K and then decreased with increasing temperature. This temperature dependence can be explained by the onset of bipolar conduction. The onset shifted to lower temperatures with increasing In content, meaning that the In filling decreases n_H and enhances the effect of minority carriers (in the present case, electrons) on the *S* at high temperatures. The *S* values of the samples with $x \leq 0.5$ were larger than those of the samples with $x \geq 0.7$, which deviates from the general relation between *S* and n_H in degenerate semiconductors. We consider that, in the samples with $x \geq 0.7$, the secondary phases such as $(Fe,Co)Sb_2$ and InSb with metallic characteristics would act as the propagation path of the charge carriers, leading to the decrease of *S*. The maximum *S* value was 146 μVK^{-1} at 705 K obtained for the sample with x = 0.5, which was close to 157 μK^{-1} at 673 K obtained for $Tl_{0.4}FeCo_3Sb_{12}$ [25]. As shown in Fig. 3.3(c), the $S^2\rho^{-1}$ values of the samples with $x \leq 0.5$ were nearly the same with each other and definitely larger than those of the samples with $x \geq 0.7$.

Figures 3.3(d) and 3.3(e) show the temperature dependences of the thermal conductivity κ and lattice thermal conductivity κ_{lat} (= $\kappa - LT\rho^{-1}$, where *L* is Lorenz number = 2.45×10^{-8} $W\Omega K^{-2}$), respectively, for polycrystalline samples with nominal compositions $In_xFeCo_3Sb_{12}$ (x = 0.3, 0.5, 0.7, and 0.9) and $In_{0.25}Fe_{1.5}Co_{2.5}Sb_{12}$ [22] for comparison, where the κ values for all samples indicate the similar trends with the κ_{lat} values. The κ_{lat} values of the samples with x = 0.3 and 0.5 were larger than the literature data of $In_{0.25}Fe_{1.5}Co_{2.5}Sb_{12}$ [22] but even lower than that of the samples with x = 0.7 and 0.9. The low κ_{lat} in the samples with x = 0.3 and 0.5 could be definitely explained by the increased grain boundaries in association with the small and uniform grains as described above. Thus, one can consider in the present case that the small and uniform grains were

more effective for the scattering of heat carrying phonons compared to the large filling fraction and existence of nanoscale precipitates. However, using of C_p=3nR is often wrong especially at high temperature where volume increases and vacancies are introduced to increase C_p. Therefore, it is the possible underestimation of the thermal conductivity in this study.

The zT values of the samples were calculated from the experimental data of S, ρ, and κ, and the results were plotted as a function of temperature (Fig. 3.3(f)). The zT values of the samples with x = 0.3 and 0.5 were slightly larger than the literature data of $In_{0.25}Fe_{1.5}Co_{2.5}Sb_{12}$ [22] due to the superior S values at high temperatures. The maximum zT value was 0.39 at 705 K obtained for the sample with x = 0.5.

Table 3.1. Lattice parameter a, sample bulk density d, and relative density % T.D. for polycrystalline samples with nominal compositions $In_xFeCo_3Sb_{12}$ (x = 0.3, 0.5, 0.7, and 0.9). The values were obtained at room temperature.

Nominal x	a (nm)	d (gcm^{-3})	T.D. (%)
0.3	0.9064(3)	7.54	98
0.5	0.9069(5)	7.68	99
0.7	0.9070(2)	7.61	-
0.9	0.9069(3)	7.79	-

Table 3.2 Chemical compositions at the skutterudite matrix-phase regions of polycrystalline

samples with nominal compositions of $In_xFeCo_3Sb_{12}$ (x = 0.3, 0.5, 0.7, and 0.9), determined by quantitative EDS analysis. All compositions show the average values obtained by repeating the point analysis at least 20 times.

Nominal composition	Chemical composition (at. %)				Chemical formula
	In	Fe	Co	Sb	
$In_{0.3}FeCo_3Sb_{12}$	1.2	4.4	18.2	76.2	$In_{0.19}Fe_{0.69}Co_{2.86}Sb_{12}$
$In_{0.5}FeCo_3Sb_{12}$	1.9	4.7	18.1	75.3	$In_{0.29}Fe_{0.74}Co_{2.89}Sb_{12}$
$In_{0.7}FeCo_3Sb_{12}$	2.7	4.4	18.6	74.3	$In_{0.43}Fe_{0.71}Co_{2.99}Sb_{12}$
$In_{0.9}FeCo_3Sb_{12}$	2.1	4.3	18.7	74.9	$In_{0.34}Fe_{0.68}Co_{3.00}Sb_{12}$

Table 3.3. Electrical resistivity ρ, Hall coefficient R_H, carrier concentration n_H, and Hall mobility μ_H obtained from the Hall measurements performed at room temperature for polycrystalline samples with nominal compositions $In_xFeCo_3Sb_{12}$ (x = 0.3, 0.5, 0.7, and 0.9) and $In_{0.25}Fe_{1.5}Co_{2.5}Sb_{12}$ [22].

Nominal x	ρ ($10^{-3}\Omega$cm)	R_H ($10^{-2}cm^3C^{-1}$)	n_H ($10^{19}cm^{-3}$)	μ_H ($cm^2V^{-1}s^{-1}$)
0.3	1.36	3.59	17	27
0.5	1.51	4.69	13	31
0.7	1.54	5.84	11	38
0.9	1.58	7.58	8	48
$In_{0.25}Fe_{1.5}Co_{2.5}Sb_{12}$ [22]	1.29	2.30	27	18

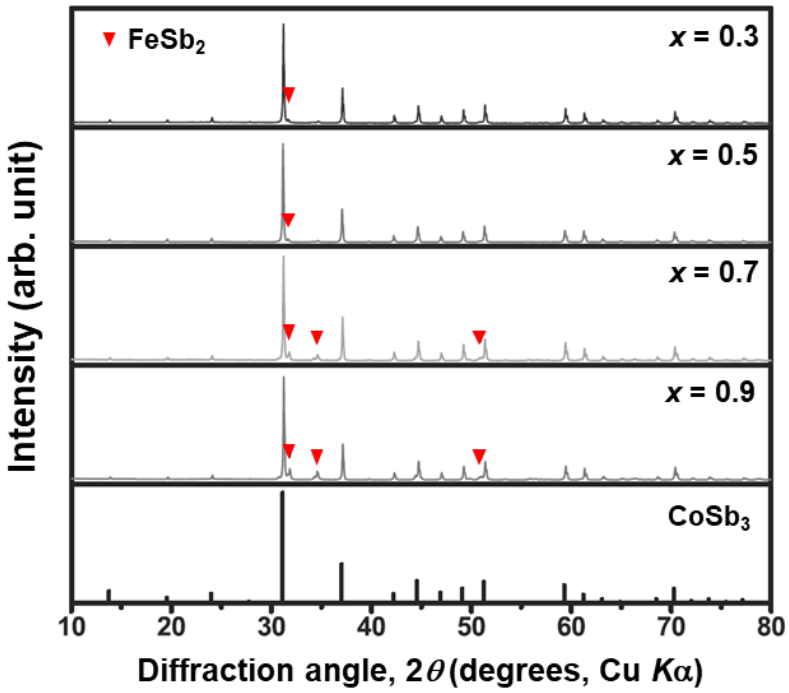

Fig. 3.1. Powder XRD patterns of polycrystalline samples of $In_xFeCo_3Sb_{12}$.

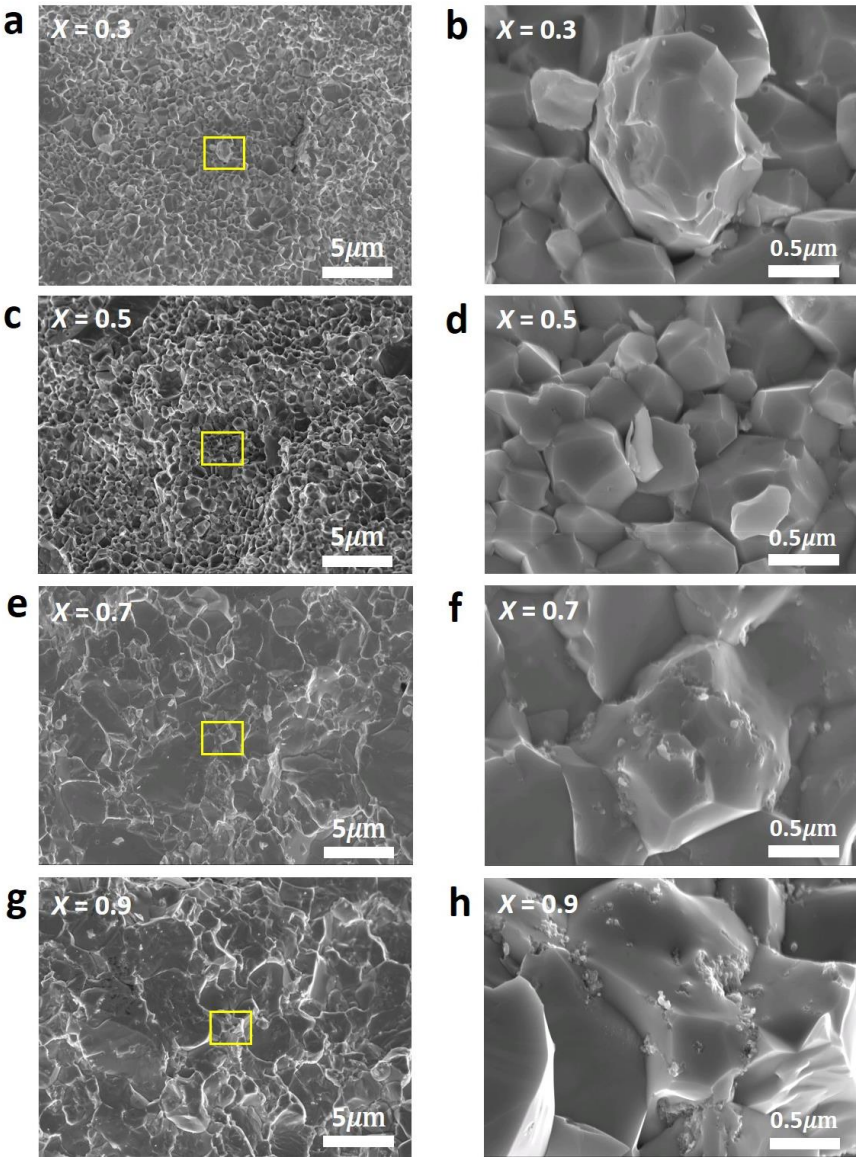

Fig. 3.2. FE-SEM images of the polycrystalline samples with nominal compositions of $In_xFeCo_3Sb_{12}$ (x = 0.3, 0.5, 0.7, and 0.9). (b), (d), (f), and (h) are the magnified images of the yellow rectangular regions in (a), (c), (e), and (g), respectively.

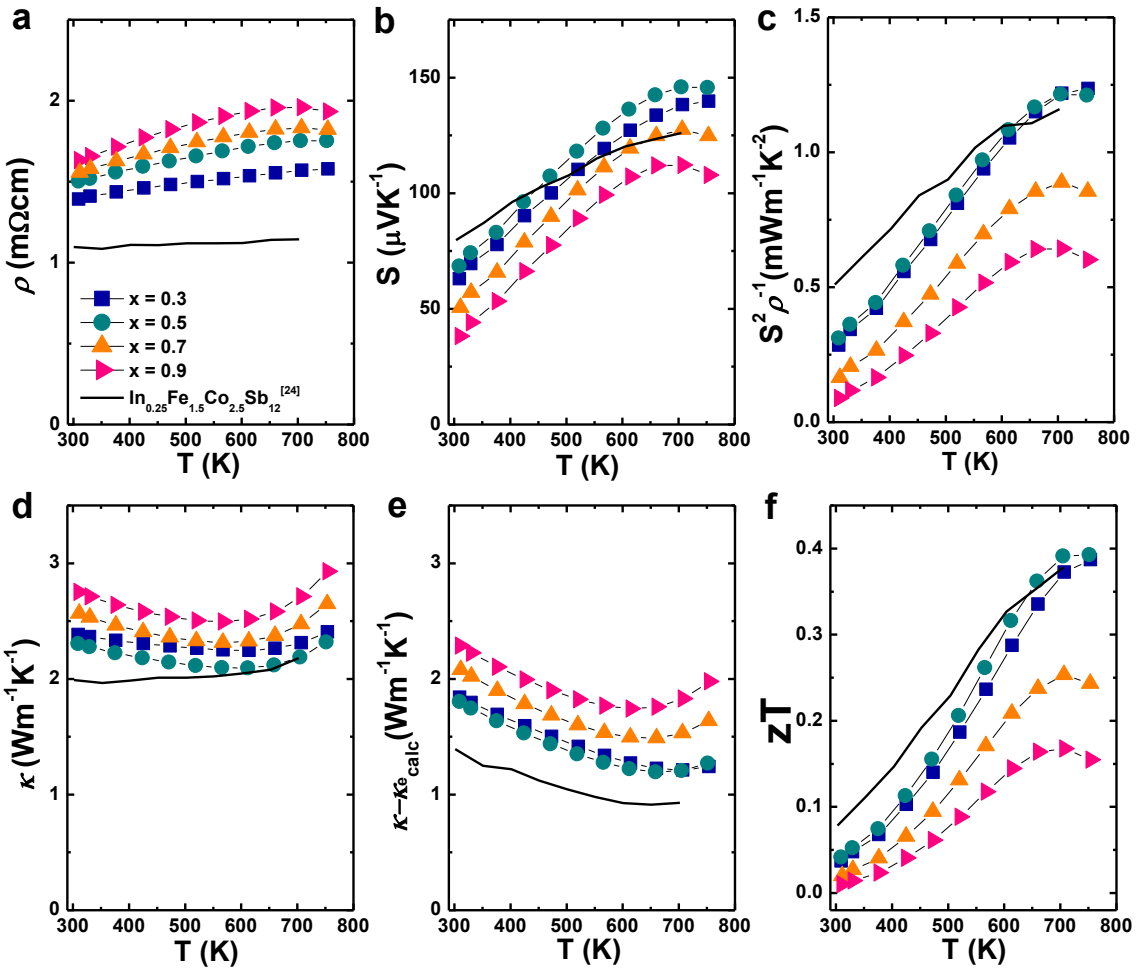

Fig. 3.3. Temperature dependences of the (a) electrical resistivity ρ, (b) Seebeck coefficient S, (c) power factor $S^2\rho^{-1}$, (d) total thermal conductivity κ, (e) lattice thermal conductivity κ-$\kappa_{e\ calc}$ (= κ - $LT\rho^{-1}$), and (f) zT for polycrystalline samples with nominal compositions $In_xFeCo_3Sb_{12}$ (x = 0.3, 0.5, 0.7, and 0.9) and $In_{0.25}Fe_{1.5}Co_{2.5}Sb_{12}$ [22].

3.3 Conclusions

The TE properties of polycrystalline samples with nominal compositions of $In_xFeCo_3Sb_{12}$ (x = 0.3, 0.5, 0.7, and 0.9) were investigated. From both the XRD and the FE-SEM/EDS analyses, the maximum filling limit of In into $FeCo_3Sb_{12}$ was confirmed between x = 0.5 and 0.7 in $In_xFeCo_3Sb_{12}$. The grain size of the samples increased with increasing x, meaning that In filling encourages the grain growth. The increase of the In content decreased the carrier concentration, which is well consistent with the simple electron counting. The samples with $x \geq 0.7$ exhibited

lower S values than those of the samples with $x \leq 0.5$, although they had lower carrier concentration. This opposite tendency is probably due to the effect of the impurity phases. The In filling and the Fe substitution as well as the small and uniform grains led to effective phonon scattering and thereby the significant reduction in the κ_{lat}. The $x = 0.5$ sample exhibited the largest power factor and the lowest κ_{lat} among the samples, thus it showed the highest zT value of 0.39 at 705 K.

3.4 References

[1] X. Zhang and L.-D. Zhao: *Journal of Materiomics* **1**, 92 (2015).

[2] S. I. Kim, K. H. Lee, H. A. Mun, H. S. Kim, S. W. Hwang, J. W. Roh, D. J. Yang, W. H. Shin, X. S. Li, Y. H. Lee, G. J. Snyder and S. W. Kim: *Science* **348**, 109 (2015).

[3] T. Plirdpring, K. Kurosaki, A. Kosuga, T. Day, S. Firdosy, V. Ravi, G. J. Snyder, A. Harnwunggmoung, T. Sugahara, Y. Ohishi, H. Muta and S. Yamanaka: *Adv. Mater.* **24**, 3622 (2012).

[4] C. Fu, S. Bai, Y. Liu, Y. Tang, L. Chen, X. Zhao and T. Zhu: *Nat. Comm.* **6**, 8144 (2015).

[5] S. Chen and Z. Ren: *Materials Today* **16**, 387 (2013).

[6] S. Wang, J. R. Salvador, J. Yang, P. Wei, B. Duan and J. Yang: *NPG Asia Mater* **8**, 285 (2016).

[7] Y. Tang, R. Hanus, S.-w. Chen and G. J. Snyder: *Nat. Comm.* **6**, 7584 (2015).

[8] G. Rogl, A. Grytsiv, P. Rogl, E. Bauer, M. Hochenhofer, R. Anbalagan, R. C. Mallik and E. Schafler: *Acta Mater.* **76**, 434 (2014).

[9] M. Rull-Bravo, A. Moure, J. F. Fernandez, and M. Martin-Gonzalez: *RSC Adv.* **5**, 41653 (2015).

[10] Y. Z. Pei, L. D. Chen, W. Zhang, X. Shi, S. Q. Bai, X. Y. Zhao, Z. G. Mei and X. Y. Li: *Appl. Phys. Lett.* **89**, 221107 (2006).

[11] Z. G. Mei, J. Yang, Y. Z. Pei, W. Zhang, L. D. Chen and J. Yang: *Phys. Rev. B* **77**, 045202 (2008).

[12] C. Artini, G. Zanicchi, G. A. Costa, M. M. Carnasciali, C. Fanciulli and R. Carlini: *Inorg. Chem.* **55**, 2574 (2016).

[13] B. Chen, J.-H. Xu, C. Uher, D. T. Morelli, G. P. Meisner, J.-P. Fleurial, T. Caillat and A. Borshchevsky: *Phys. Rev. B* **55**, 1476 (1997).

[14] Y. Dong, P. Puneet, T. M. Tritt and G. S. Nolas: *J. Solid State Chem.* **209**, 1 (2014).

[15] D. R. Thompson, C. Liu, J. Yang, J. R. Salvador, D. B. Haddad, N. D. Ellison, R. A. Waldo and J. Yang: *Acta Mater.* **92**, 152 (2015).

[16] R. Liu, J. Yang, X. Chen, X. Shi, L. Chen and C. Uher: *Intermetallics* **19**, 1747 (2011).

[17] Y. Tang, Y. Qiu, L. Xi, X. Shi, W. Zhang, L. Chen, S.-M. Tseng, S.-w. Chen and G. J. Snyder: *Energy & Environ. Science* **7**, 812 (2014).

[18] W. Zhao, P. Wei, Q. Zhang, H. Peng, W. Zhu, D. Tang, J. Yu, H. Zhou, Z. Liu, X. Mu, D. He, J. Li, C. Wang, X. Tang and J. Yang: *Nat. Comm.* **6**, 6197 (2015).

[19] K. Kurosaki, G. Li, Y. Ohishi, H. Muta and S. Yamanaka: *Front. Chem.* **2**, 84 (2014).

[20] X. Shi, J. Yang, L. Wu, J. R. Salvador, C. Zhang, W. L. Villaire, D. Haddad, J. Yang, Y. Zhu and Q. Li: *Scientific Reports* **5**, 14641 (2015).

[21] J. Leszczynski, A. Dauscher, P. Masschelein and B. Lenoir: *J. Elec. Mater.* **39**, 1764 (2010).

[22] K.-H. Park, J.-Y. Jung, S.-C. Ur and I.-H. Kim: *J. Elec. Mater.* **39**, 1750 (2010).

[23] W. Zhao, P. Wei, Q. Zhang, C. Dong, L. Liu and X. Tang: *J. Am. Chem. Soc.* **131**, 3713 (2009).

[24] E. Visnow, C. P. Heinrich, A. Schmitz, J. de Boor, P. Leidich, B. Klobes, R. P. Hermann, W. E. Müller and W. Tremel: *Inorg. Chem.* **54**, 7818 (2015).

[25] D. Kim, K. Kurosaki, Y. Ohishi, H. Muta and S. Yamanaka: *APL Mater.* **1**, 032115 (2013).

CHAPTER IV

Thermoelectric Properties of Ce Single-Filled *p*-type Skutterudites

$CoSb_3$-based filled skutterudites are known as good *n*-type thermoelectric (TE) materials. However, the *p*-type ones have not been intensively investigated. In this study, we focus on Ce-filled Fe-substituted $CoSb_3$ as *p*-type skutterudites, where Fe will act as a hole dopant. Polycrystalline samples with nominal compositions of $Ce_xFe_yCo_{4-y}Sb_{12}$ (x = 0.8, 0.9, 1.0 and y = 3.0, 3.5) are synthesized and the high temperature TE properties are investigated. All the samples show the *p*-type conduction as we expected. It is found that the samples with y = 3.5 exhibit clearly lower κ_{lat} values than those of the samples with y = 3.0, meaning that the Fe/Co substitution is more predominant than the Ce filling for the κ_{lat} reduction. The maximum zT value observed in this study is 0.78 at 704 K for the sample with x = 1.0, y = 3.5, which is close to the best value reported so far for Ce-filled Fe-substituted $CoSb_3$-based *p*-type skutterudites.

4.1 Introduction

In the present study, we show the enhancement of the zT of Ce-filled *p*-type skutterudites $Ce_xFe_yCo_{4-y}Sb_{12}$ by tuning both the Fe/Co ratio and the Ce filling fraction. Furthermore, we show that the Fe/Co substitution is more predominant than the Ce filling for the κ_{lat} reduction in the $Ce_xFe_yCo_{4-y}Sb_{12}$ system.

4.2 Results and Discussion

The powder XRD patterns of the SPS bulk samples are shown in Figure 4.1. It is confirmed that all samples consist mainly of the skutterudite phase. A negligible amount of the $FeSb_2$ phase is observed as the secondary phase in the samples except for the samples with $x \geq 0.9$, y = 3.0. The peak intensity of the secondary phase decreases with increasing x. The lattice parameter, a, of the skutterudite phase calculated from the XRD patterns and the density values of the SPS bulk samples are summarized in Table 4.1. The a values of the samples with y = 3.5 are clearly larger than those of the samples with y = 3.0 when the Ce content, x, is the same. This is due to the larger ionic radius of Fe^{2+} (0.074 nm) than that of Co^{3+} (0.063 nm).[29] The a value of the sample with x = 1.0, y = 3.0 is 0.9110(3) nm, which is in good agreement with the literature values for the skutterudite having the same nominal composition (a = 0.9103 - 0.9115 nm) [30-33]. On the other

hand, the a value of the sample with x = 1.0, y = 3.5 is 0.9120(2) nm, which is slightly lower than the literature value for the skutterudite having the same nominal composition (a = 0.9127 nm) [30,32]. The density of all the samples are above 97% of the theoretical density.

Figure 4.2 shows the FE-SEM images of the freshly broken surface of the SPS bulk samples (x = 0.8, 1.0 and y = 3.0, 3.5). It can be confirmed that the samples are dense without showing any remarkable cracks or pores. The sample with x = 0.8, y = 3.0 is composed of dense grains and precipitates with the sizes of approximately 10 μm and several hundred nm, respectively. The precipitates are observed at the surface of the grains. Although the spatial resolution of the EDS analysis prevents us to evaluate the composition of the precipitates quantitatively, we predict that these precipitates are $FeSb_2$ based on the XRD results. The formation of $FeSb_2$ nanoparticles in the p-type $(Co,Fe)Sb_3$-based skutterudite samples has been reported in the previous papers [34]. On the other hand, as shown in Figure 4.2(d), no such precipitates are observed on the grains of the sample with x = 1.0, y = 3.0. This means that the amount of the substituted Fe increases due to the effect of the charge compensation caused by the introduction of higher amount of the filling atom. The chemical compositions of the SPS bulk samples determined by the quantitative EDS analyses are summarized in Table 4.2. The data are the average values of the point analyses performed at more than 10 different grains. The Ce content in the skutterudite phase increases with increasing x for both series of the samples with y = 3.0 and y = 3.5. Furthermore, the Ce content of the samples with y = 3.5 is larger than that of the samples with y = 3.0, meaning that Fe substitution for Co leads to the higher value of the maximum Ce content. In the present case, the actual Ce content of the sample with x = 1.0, y = 3.5 is ~0.90, slightly higher than the literature value for the skutterudite having the same nominal composition (~0.85) [32].

Table 4.3 summarizes the electrical resistivity ρ, Hall coefficient R_H, Hall carrier concentration n_H, and Hall mobility μ_H of the SPS bulk samples. The data for $CeFe_3CoSb_{12}$ [35] are shown for comparison. All samples show the p-type conduction. The n_H values of the samples with y = 3.5 is larger than those of the samples with y = 3.0. Moreover, the n_H values decrease with increasing the Ce content. These results can be explained by the simple carrier counting, i.e. the Fe substitution leads to hole doping while the Ce filling leads to positive charge compensation by electron doping. These results suggest that the carrier concentration of p-type $Ce_xFe_yCo_{4-y}Sb_{12}$ can be controlled by tuning both the Fe/Co ratio and the Ce filling fraction. The μ_H values of the samples with y = 3.5 is lower than those of the samples with y = 3.0. On the other hand, when the y values are the same, the μ_H values are similar independent of the Ce content. This implies that,

in the investigated range, the Ce filling has no significant influence on the carrier mobility in *p*-type $Ce_xFe_yCo_{4-y}Sb_{12}$.

Figures 4.3(a), 4.3(b), and 4.3(c) show the temperature dependences of ρ, S, and $S^2\rho^{-1}$, respectively, for the SPS bulk samples. These data are obtained by the ZEM-3 measurement. The literature data for $Ce_{0.8}Fe_3CoSb_{12}$ [33] are also shown for comparison. Both the ρ and S of the samples increase with increasing temperature, indicating a typical behavior for metals or degenerated semiconductors. The samples with y = 3.5 show lower ρ and S compared with the samples with y = 3.0. Generally, in case of point scattering effect by substitution, it has the best effect on 50 % of displacement for thermal conductivity. However, this study shows the opposite results, and this trend can be found in other papers although in no clear explanation for the reasons [28]. Furthermore, the ρ and S increase with increasing the Ce content x in all cases. These results can be simply explained from the carrier concentration as summarized in Table 4.3, where the n_H values of the samples with y = 3.5 are clearly higher than those of the samples with y = 3.0, and the n_H values of all samples decrease with increasing the x value when the y values are the same. The S of all samples monotonically increase with temperature up to around 700 K and then start to decrease after reaching a maximum. One of the reasons for the reduction of S at high temperature is the onset of a bipolar conduction. The maximum S value is ~180 μV K^{-1} at 704 K obtained for the sample with x = 1.0, y = 3.0, which is close to the literature value for the skutterudite having the same nominal composition (~180 μV K^{-1} at 704 K) [32]. As shown in Fig. 4.3(c), the $S^2\rho^{-1}$ values of the samples with y = 3.5 are slightly higher than those of the samples with y = 3.0. The sample with x = 1.0, y = 3.5 shows the maximum $S^2\rho^{-1}$ of 2.6 mW / mK^2 at 704 K.

Temperature dependences of the κ and κ_{lat} ($= \kappa - \kappa_{el}$) for the SPS bulk samples are shown in Figures 4.3(d) and 4.3(e), respectively. The Wiedemann–Franz law ($\kappa_{el} = LT\rho^{-1}$) was applied to estimate the κ_{el}, where $L = 1.5 + \exp[-|S|/116]$ WΩK^{-2} was used [37]. As shown in Fig. 4.3(d), the κ values for the samples with y = 3.5 are much lower than those of the samples with y = 3.0. However, above the room temperature, carrier-phonon interaction has negligibly small effect. And also, at high temperature, phonon-phonon Umklapp decreases exponentially. Therefore, more research is needed because there is obvious that the substitution of Fe has affected the reduction of thermal conductivity. Moreover, the similar trend is also shown in the κ_{lat} (Fig. 4.3(e)). On the other hand, when the y values are the same, the κ_{lat} values are similar independent of the Ce content. These results indicate that the Fe/Co substitution is more predominant than the Ce filling for the κ_{lat} reduction in the $Ce_xFe_yCo_{4-y}Sb_{12}$ system. The κ_{lat} of all samples reach minimum values around

700 K, and then increase slightly at high temperature, due to the bipolar effect which is also observed in the temperature dependence of S (Fig. 4.3(b)). The minimum κ_{lat} value is ~0.99 $Wm^{-1}K^{-1}$ at 750 K obtained for the sample with $x = 0.8$, $y = 3.5$.

The zT values of the samples evaluated from the measured TE properties are shown in Figure 4.3(f). The zT values of the samples with $y = 3.5$ are clearly higher than those of the samples with $y = 3.0$, which is due to the lower κ_{lat} of the samples with $y = 3.5$ in spite of the similar $S^2\rho^{-1}$ values in the $y = 3.0$ and 3.5 samples. The maximum zT value observed in this study is 0.78 at 704 K for the sample with $x = 1.0$, $y = 3.5$, which is close to the best value reported so far for Ce-filled Fe-substituted $CoSb_3$-based p-type skutterudites (~0.88 at 700 K) [36]. In addition to the evaluated zT_{max}, we also evaluated zT_{eng} [38] of the SPS bulk samples with nominal compositions $Ce_xFe_yCo_{4-y}Sb_{12}$ ($x = 0.8$, 0.9, 1.0 and $y = 3.0$, 3.5), where the cold side temperature T_c was set as 373 K. The results are shown in Fig. 4.4, where the literature data [29] are also shown for comparison. The sample of $x = 1.0$, $y = 3.5$ exhibits the highest values not only in zT_{max} but also in zT_{eng}. The maximum zT_{eng} is 0.39 at $\Delta T = 331$ K, which is slightly higher than the literature data [29].

Table 4.1. Lattice parameter of the skutterudite phase and density of the SPS bulk samples of $Ce_xFe_yCo_{4-y}Sb_{12}$ ($x = 0.8$, 0.9, 1.0 and $y = 3.0$, 3.5).

Nominal composition	a (nm)	Density ($g \cdot cm^{-3}$)		Relative Density (% T. D.)
		Theoretical	Experimental	
$Ce_{0.8}Fe_{3.0}Co_{1.0}Sb_{12}$	0.9100(3)	7.81	7.75	99
$Ce_{0.9}Fe_{3.0}Co_{1.0}Sb_{12}$	0.9107(1)	7.91	7.73	98
$Ce_{1.0}Fe_{3.0}Co_{1.0}Sb_{12}$	0.9110(3)	8.05	7.81	97
$Ce_{0.8}Fe_{3.5}Co_{0.5}Sb_{12}$	0.9118(3)	7.88	7.64	97
$Ce_{0.9}Fe_{3.5}Co_{0.5}Sb_{12}$	0.9119(5)	7.92	7.76	98
$Ce_{1.0}Fe_{3.5}Co_{0.5}Sb_{12}$	0.9120(2)	7.98	7.82	98

Table 4.2. Chemical compositions of the skutterudite phase regions of the SPS bulk samples with the nominal compositions of $Ce_xFe_yCo_{4-y}Sb_{12}$ (x = 0.8, 0.9, 1.0 and y = 3.0, 3.5). The chemical composition is determined by the quantitative EDS analysis, where all the data are the average values obtained by repeating the point analyses at least 20 times.

Nominal composition	Results of the quantitative EDS analysis (at. %)				Chemical composition
	Ce	Fe	Co	Sb	
$Ce_{0.8}Fe_{3.0}Co_{1.0}Sb_{12}$	4.4	17.2	6.4	72.0	$Ce_{0.75}Fe_{2.88}Co_{1.07}Sb_{12.10}$
$Ce_{0.9}Fe_{3.0}Co_{1.0}Sb_{12}$	4.9	17.5	5.9	71.7	$Ce_{0.83}Fe_{2.96}Co_{1.00}Sb_{12.11}$
$Ce_{1.0}Fe_{3.0}Co_{1.0}Sb_{12}$	5.1	17.9	5.4	71.6	$Ce_{0.87}Fe_{3.04}Co_{0.92}Sb_{12.16}$
$Ce_{0.8}Fe_{3.5}Co_{0.5}Sb_{12}$	4.5	21.1	3.0	71.4	$Ce_{0.76}Fe_{3.55}Co_{0.50}Sb_{11.99}$
$Ce_{0.9}Fe_{3.5}Co_{0.5}Sb_{12}$	4.9	20.3	3.2	71.6	$Ce_{0.82}Fe_{3.55}Co_{0.54}Sb_{11.99}$
$Ce_{1.0}Fe_{3.5}Co_{0.5}Sb_{12}$	5.1	20.0	3.2	71.7	$Ce_{0.90}Fe_{3.55}Co_{0.55}Sb_{12.00}$

Table 4.3. Electrical resistivity ρ, Hall coefficient R_H, Hall carrier concentration n_H, and Hall mobility μ_H of the SPS bulk samples with the nominal compositions of $Ce_xFe_yCo_{4-y}Sb_{12}$ (x = 0.8, 0.9, 1.0 and y = 3.0, 3.5). All the data are obtained at room temperature. The data for $CeFe_3CoSb_{12}$ [35] are shown for comparison.

Nominal composition	ρ ($10^{-4}\Omega$cm)	R_H ($10^{-2}cm^3C^{-1}$)	n_H ($10^{20}cm^{-3}$)	μ_H ($cm^2V^{-1}s^{-1}$)
$Ce_{0.8}Fe_{3.0}Co_{1.0}Sb_{12}$	8.15	4.69	1.3	58
$Ce_{0.9}Fe_{3.0}Co_{1.0}Sb_{12}$	9.06	5.77	1.1	64
$Ce_{1.0}Fe_{3.0}Co_{1.0}Sb_{12}$	10.3	6.96	0.9	67
$Ce_{0.8}Fe_{3.5}Co_{0.5}Sb_{12}$	5.53	2.13	2.9	42
$Ce_{0.9}Fe_{3.5}Co_{0.5}Sb_{12}$	6.16	2.61	2.4	42
$Ce_{1.0}Fe_{3.5}Co_{0.5}Sb_{12}$	6.99	3.08	2.0	49
$CeFe_3CoSb_{12}$[35]	7.69	2.33	2.7	-

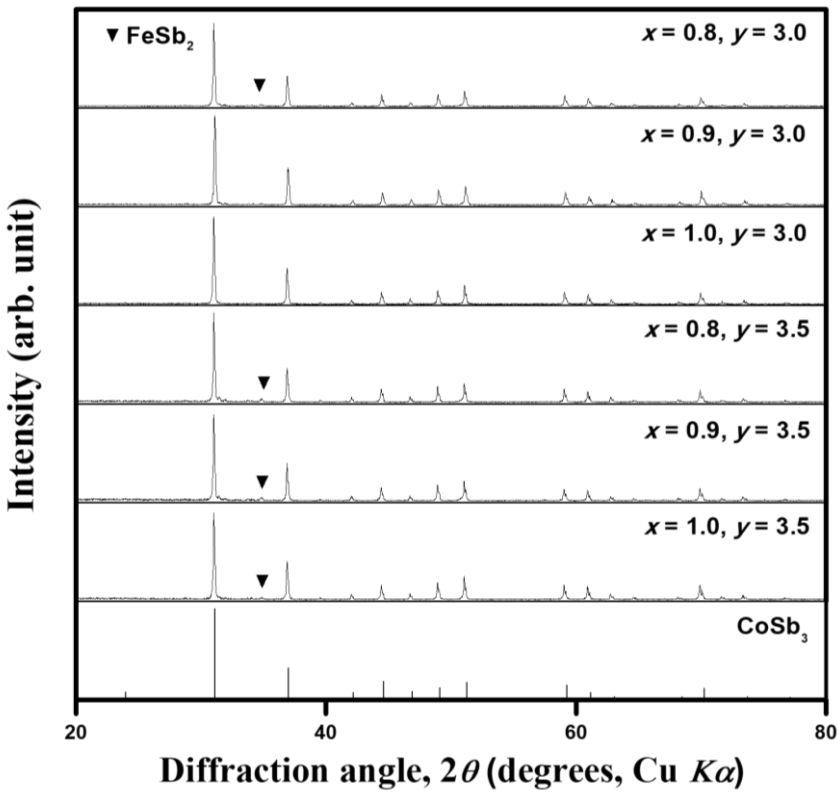

Fig. 4.1. Powder XRD patterns of the SPS bulk samples of $Ce_xFe_yCo_{4-y}Sb_{12}$ (x = 0.8, 0.9, 1.0 and y = 3.0, 3.5).

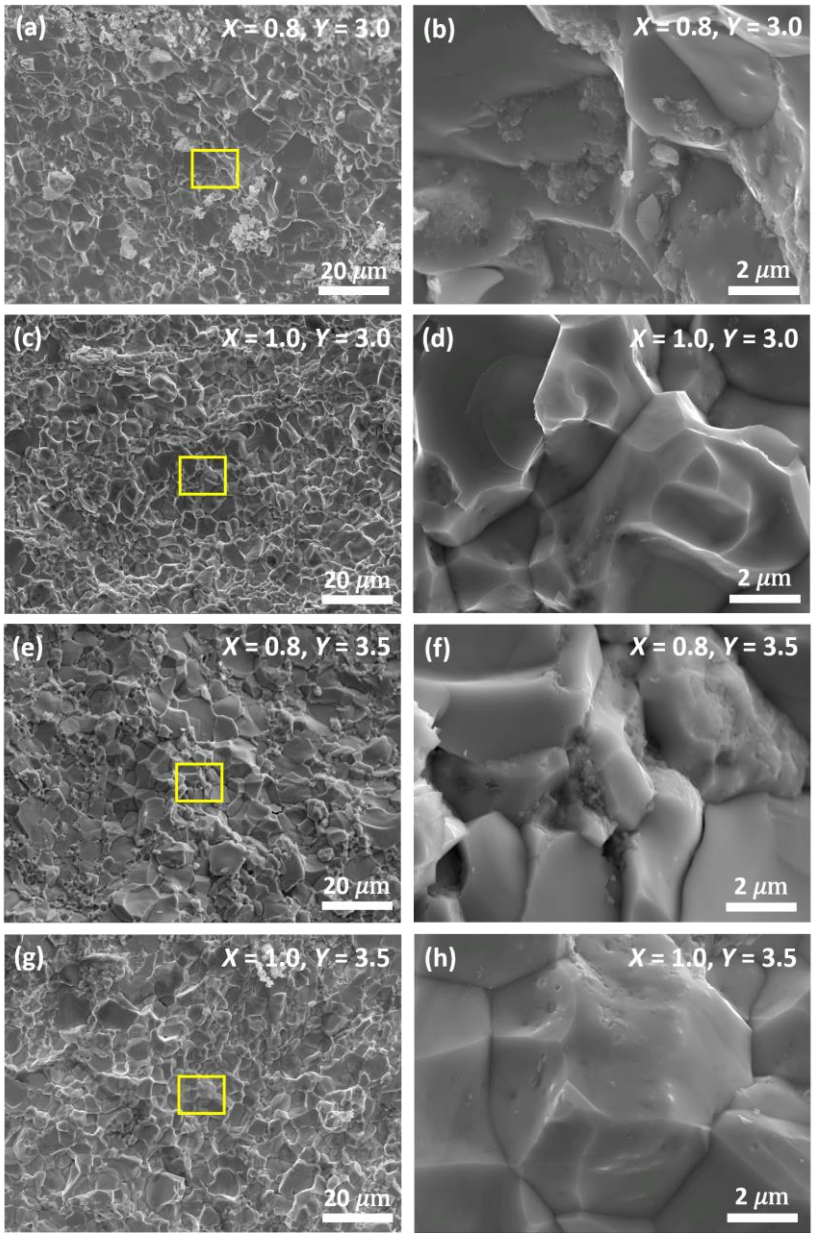

Fig. 4.2. FE-SEM images of the broken surface of the SPS bulk samples with the nominal compositions of x = 0.8, 1.0 and y = 3.0, 3.5 in $Ce_xFe_yCo_{4-y}Sb_{12}$.

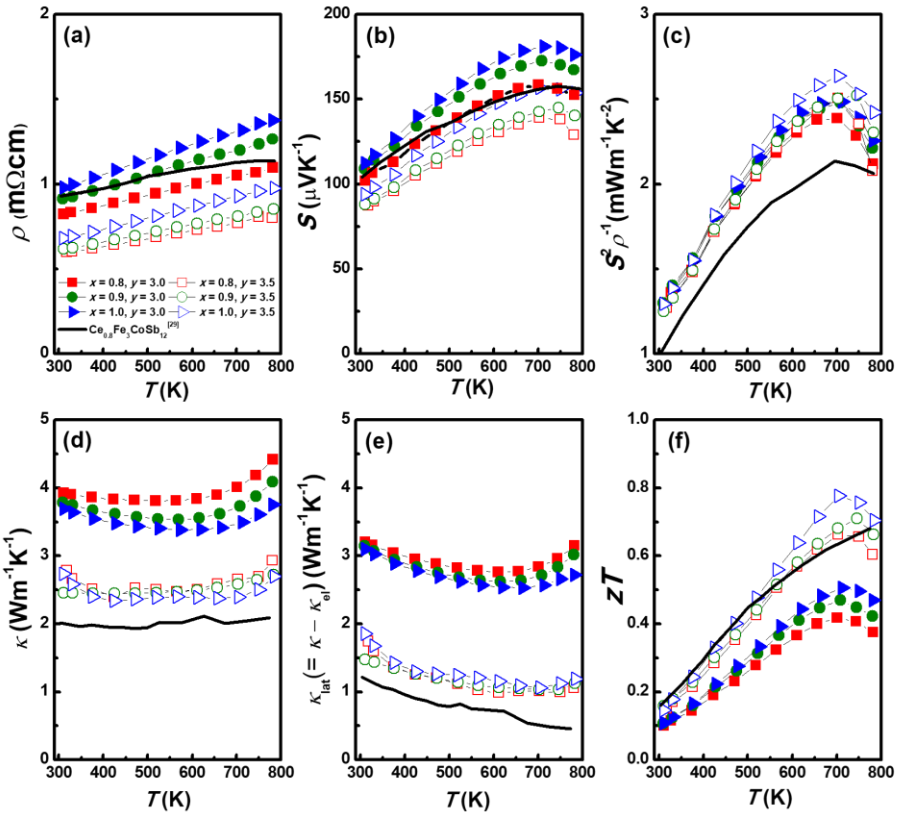

Fig. 4.3. Temperature dependences of the (a) electrical resistivity ρ, (b) Seebeck coefficient S, (c) power factor $S^2\rho^{-1}$, (d) total thermal conductivity κ, (e) lattice thermal conductivity κ_{lat} ($= \kappa - \kappa_{el}$), and (f) zT of the SPS bulk samples with nominal compositions $Ce_xFe_yCo_{4-y}Sb_{12}$ (x = 0.8, 0.9, 1.0 and y = 3.0, 3.5). The literature data for $Ce_{0.8}Fe_3CoSb_{12}$ [29] are shown for comparison.

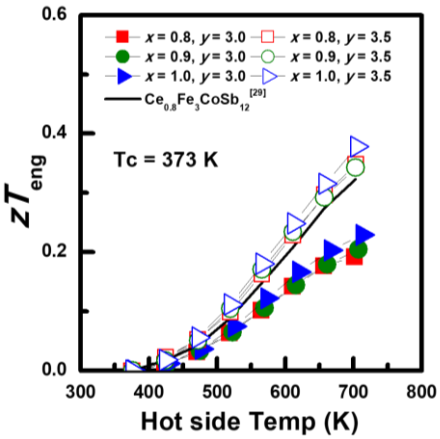

Fig. 4.4. zT_{eng} [38] of the SPS bulk samples with nominal compositions $Ce_xFe_yCo_{4-y}Sb_{12}$ (x = 0.8, 0.9, 1.0 and y = 3.0, 3.5). The literature data for $Ce_{0.8}Fe_3CoSb_{12}$ [29] are shown for comparison.

4.3 Conclusions

Ce-filled *p*-type skutterudites $Ce_xFe_yCo_{4-y}Sb_{12}$ (x = 0.8, 0.9, 1.0 and y = 3.0, 3.5) were prepared and their TE properties were evaluated from room temperature to 773 K. All samples were mainly composed of the skutterudite phase and showed the *p*-type conduction. The hole carrier concentration increased with increasing the Fe content, while decreased with increasing the Ce filling fraction. Thus, the carrier concentration was optimized by tuning the Fe/Co ratio and the Ce filling fraction. The κ_{lat} values were similar independent of the Ce filling faction, when the Fe/Co ratio is the same. On the other hand, the samples with y = 3.5 exhibited clearly lower κ_{lat} values than those of the samples with y = 3.0. The present study revealed that the Fe/Co substitution is more predominant than the Ce filling for the κ_{lat} reduction and the best composition is x = 1.0, y = 3.5 in $Ce_xFe_yCo_{4-y}Sb_{12}$, showing the maximum zT values of 0.78 at 704 K.

4.4 References

[1] Terry M. Tritt, *Annu. Rev. Mater. Sci.* **41**, 433 (2011).

[2] W. He, G. Zhang, X. Zhang, J. Ji, G. Li and X. Zhao, *Appl. Energy* **143**, 1 (2015).

[3] G. J. Snyder and Eric S. Toberer, *Nat. Mater.* **7**, 105 (2008).

[4] Jian He, Terry M. Tritt, *Science* **357**, 6358 (2017).

[5] T. Zhu, C. Fu, H. Xie, Y. Liu, and X. Zhao, Adv. *Energy Mater.* **5**, 1500588 (2015).

[6] W. Silpawilawan, K. Kurosaki, Y. Ohishi, H. Muta and S. Yamanaka, *J. Mater. Chem. C* **5**, 6677 (2017).

[7] W. Li, S. Lin, M. Weiss, Z. Chen, J. Li, Y. Xu, W. G. Zeier and Y. Pei, *Adv. Energy Mater.* 1800030 (2018).

[8] S. Wang, J. Yang, L. Wu, P. Wei, W. Zhang and J. Yang, *Adv. Funct. Mater.* **25**, 6660 (2015).

[9] Y. Li, P. Qiu, H. Duan, J. Chen, G. J. Snyder, X. Shi, B. B. Iversen and L. Chen, *J. Mater. Chem. C.* **4**, 4374 (2016).

[10] J. Kim, K. Kurosaki, S. Choi, Y. Ohishi, H. Muta, S. Yamanaka, M. Takahashi and Y. Tanaka, *Mater. Trans.* **58**, 8, 1207 (2017).

[11] B. C. Sales, D. Mandrus and R. K. Williams, *Science* **272**, 5266 (1996).

[12] W. Zhang, X. Shi, G. Mei, Y. Xu, L. D. Chen, J. Yang and G. P. Meisner, *Appl. Phys. Lett.* **89**, 112105 (2006).

[13] Z. G. Mei, Jiong Yang, Y. Z. Pei, W. Zhang, and L. D. Chen and Jihui Yang, *Phys. Rev. B* **77**,

045202 (2008).

[14] K. Kurosaki, G. Li, Y. Ohishi, H. Muta and S. Yamanaka, *Front. Chem.* **2** 84 (2014).

[15] Y. Tang, Y. Qiu, L. Xi, X. Shi, W. Zhang, L. Chen, S. M. Tseng, S. W. Chen and G. J. Snyder, *Energy Environ. Sci.* **7**, 812 (2014).

[16] L. Xi, Y. Qui, S. Zheng, X. Shi, Jiong Yang, L. Chen, D. J. Singh, Jihui Yang and W. Zhang, *Acta Mater.* **85**, 112-121 (2015).

[17] S. Choi, K. Kurosaki, G. Li, Y. Ohishi, H. Muta and S. Yamanaka, *AIP Adv.* **6**, 125015 (2016).

[18] S. Bao, J. Yang, J. Peng, W. Zhu, X. Fan and X. Song, *J. Alloys Compd.* **421**, 105-108 (2006).

[19] C. Zhou, D. Morelli, X. Zhou, G. Wang and C. Uher, *Intermetallics* **19**, 1390-1393 (2011).

[20] S. Choi, K. Kurosaki, Y. Ohishi, H. Muta and S. Yamanaka, *J. Appl. Phys.* **115**, 023702 (2014).

[21] Y. Li, P. Qui, H. Duan, J. Chen, G. J. Snyder, X. Shi, B. B. Iversen and L. Chen, *J. Mater. Chem. C* **4**, 4374 (2016).

[22] S. Ballikaya, N. Uzar, S. Yildirim. J. R. Salvador and C. Uher, *J. Solid State Chem.* **193**, 31 (2012).

[23] H. Li, X. Su. X. Tang, Q. Zhang, C. Uher. G. J. Snyder and U. Aydemir, *J. Materiomics* **3**, 273 (2017).

[24] Y. Yan, W. Wong-Ng, L. Li, I. Levin, J. Kaduk, M. Suchomel, X. Sun, G. Tan and X. Tang, *J. Solid State Chem.* **218**, 221 (2014).

[25] P. Lu, F. Wu, H. Han, Q. Wang, Z. Shen and X. Hu, *J. Alloys Comp.* **505**, 255 (2010).

[26] D. Thompson, C. Liu, J. Yang, J. Salvador, D. Haddad, N. Ellison, R. Waldo and J. Yang, *Acta Mater.* **92**, 152 (2015).

[27] K. Wei, Y. Dong, P. Puneet, T. Tritt and G. Nolas, *J. Alloys Comp.* **614**, 330 (2014).

[28] T. Dahal, H. Kim, S. Gahlawat, K. Dahal, Q. Jie, W. Liu, Y. Lan, K. White and Z. Ren, *Acta Mater.* **117**, 13 (2016).

[29] X. Tang and Q. Zhang, *J. Appl. Phys.* **97**, 093712 (2005)

[30] G. P. Meisner, D. T. Morelli, S. Hu, J. Yang and C. Uher, *Phys. Rev. B* **80**, 16 (1998).

[31] D. Berardan, C. Godart, E. Alleno, E. Leroy and P. Rogl, *J. Alloys Comp.* **350**, 30 (2003).

[32] P. F. Qiu, R. H. Liu, J. Yang, X. Shi, X. Y. Huang. W. Zhang, L. D. Chen, Jihui Yang and D. J. Singh, *J. Appl. Phys.* **111**, 023705 (2012).

[33] J. Gonjal, P. Vaqueiro, C. Nuttall, R. Potter, A. V. Powell, *J. Alloys Comp.* **695**, 3598 (2017).

[34] D. Morelli and G. Meisner, *J. Appl. Phys.* **77**, 3777 (1995).

[35] X.Tang, L. Chen, T. Goto and T. Hirai, *J. Mater. Res.* **16**, 3 (2001)

[36] R. Liu, P. Qiu, X. Chen, X. Huang and L. Chen, *J. Mater. Res.* **26**, 15 (2011).

[37] H. Kim, Z. Gibbs, Y. Tang, H. Wang and G. Snyder, *APL Mater.* **3**, 041506 (2015).

[38] H. Kim, W. Liu, G. Chen, C. Chu and Z. Ren, *Proc. Natl. Acad. Sci.* **112**, 8205 (2015).

CHAPTER V

Thermoelectric Properties of Ga and Ce Double-Filled *p*-type Skutterudites

Among the *p*-type filled skutterudites, Ce single-filled $(Co,Fe)Sb_3$ is known as a promising thermoelectric material. Here, we try to enhance the thermoelectric properties of Ce-filled $(Co,Fe)Sb_3$ by co-filling of Ga. We synthesize the samples in the nominal compositions $Ga_xCeFe_{3.5}Co_{0.5}Sb_{12-x/3}$ (x = 0.06, 0.09, 0.15, and 0.21) and examined their thermoelectric properties from room temperature to 773 K. It is confirmed that Ga can occupy not only the void site but also the Sb site, i.e., the chemical formula can be expressed as $(Ga_{VF})_{2x/3}CeFe_{3.5}Co_{0.5}Sb_{12-x/3}(Ga_{Sb})_{x/3}$, where Ga_{VF} and Ga_{Sb} mean Ga in the void and Sb sites, respectively. Ga contributes to optimize the carrier concentration as well as to reduce the lattice thermal conductivity. Owing to these Ga contributions, the material's thermoelectric figure of merit zT is enhanced and reaches 0.85 in maximum at 773 K, which is obtained for the sample with x = 0.15.

5.1 Introduction

Thermoelectric (TE) power generation enables a direct conversion from waste heat to electricity based on the Seebeck effect of TE materials. TEs are considered to be utilized in wide applications such as waste heat recovery in automobiles [1,2]. The energy conversion efficiency of TEs is determined by performance of the TE materials called material's dimensionless figure of merit, defined as, $zT = S^2\sigma T/\kappa$, where S, σ, T, and κ are the Seebeck coefficient, electrical conductivity, absolute temperature, and total thermal conductivity, respectively. $S^2\sigma$ is called as power factor. Normally, κ consists of an electronic (κ_{el}) and a lattice part (κ_{lat}), i.e., $\kappa = \kappa_{el}+\kappa_{lat}$. S, σ, and κ_{el} are intimately related with each other as a function of carrier concentration of a given material, which is a major obstacle to enhance the zT. On the other hand, κ_{lat} is independent of the carrier concentration, thus, many researchers have tried to minimize the κ_{lat} for enhancement of the zT [3-6].

Skutterudite compounds show good TE performance at intermidiate temperature range. The crystal structure of skutterudites such as $CoSb_3$ contains two large interstitial voids per unit cell, [7,8] where various elements, such as rare earths elements, [9-12] alkaline metals, [13,14] and

group 13 elements [15-18] can be introduced to form filled skutterudites. Notably the filler elements inserted in the voids rattle and act as an effective scattering source for heat carrying phonons leading to the κ_{lat} reduction. They also act as electron donors to make *n*-type skutterudites and help adjusting the carrier concentration to optimize the power factor. Meanwhile, *p*-type ones can be made by substituting transition metals, such as Fe substitution with Co in $CoSb_3$ [9,11,18-20].

Although similar performance in both *n*- and *p*-type TE materials is required for a powerful TE module, *p*-type skutterudites show lower TE performance than *n*-type ones normally. For example, $R(Co,Fe)_4Sb_{12}$-based single-filled *p*-type skutterudites, where *R* represents a filler element, present small Seebeck coefficient and carrier mobility compared with those of *n*-type RCo_4Sb_{12}. It has been reported that by increasing the filling fraction of *R* in $R(Co,Fe)_4Sb_{12}$, the hole concentration is suppressed by electron doping, leading to the increase in the *S* but decrease in the σ [20,21]. As a result, $S^2\sigma$ can't be enhanced and remains at a low value [10,22-24].

Recently, double-filled or multiple-filled skutterudites have been investigated [25,26]. In many cases, double-filled skutterudites exhibit higher *zT* values than single-filled ones. On the other hand, it has been reported that Ga can be a good filler element for *n*-type RCo_4Sb_{12} [27-29]. In addition, it has been found that besides the void site, Ga can occupy the Sb site too, in n-type filled skutterudites [30].

Here, we investigate the effect of Ga on the TE properties of *p*-type $(Co,Fe)_4Sb_{12}$-based double-filled skutterudites. Ce is selected as the first filler element, because Ce single-filled *p*-type skutterudites show relatively good TE properties [26,31,32]. Then, Ga is selected as the second filler element to make Ga and Ce double-filled *p*-type skutterudites. Samples with the nominal compositions $Ga_xCeFe_{3.5}Co_{0.5}Sb_{12-x/3}$ (x = 0.06, 0.09, 0.15, and 0.21) are synthesized and their TE properties are examined from room temperature to 773 K.

5.2 Results and Discussion

Figure 5.1 shows the powder XRD patterns of the SPS bulk samples. It can be confirmed from the XRD patterns that the main phase of all the samples are the skutterudite phase. The lattice parameters of the SPS bulk samples are listed in Table 5.1, showing that the lattice parameter increases with increasing x in $Ga_xCeFe_{3.5}Co_{0.5}Sb_{12-x/3}$ except for x = 0.21. Generally, Ga and Ce filling into the voids expands the lattice parameter of the skutterudite structure [28,32]. On the other hand, the substitution of Ga with the Sb site tends to shrink the lattice [29]. Thus, the increase in

the lattice parameter observed in this study implies that the Ga void-filling is more predominant than the Ga substitution with Sb site. Actually, Xi et al. have reported that the ratio of Ga atoms at the void site to those at the Sb sites for Ga-added *n*-type $CoSb_3$ is very close to be 2:1 [30]. As summarized in Table 5.1, the densities of all samples are over 96% of the theoretical values.

Figure 5.2 shows the FE-SEM images of the broken surface of the SPS bulk samples. Dense structures without any cracks or pores are observed. The grain sizes are around ~10 μm. Although small amounts of nanoscale precipitates have been observed in Ce single-filled *p*-type $Fe_{3.5}Co_{1.5}Sb_{12}$ after exceeding the filling limit of Ce, [31,33] no such precipitates are observed in the present case. Substitutions of Fe with Co increases the lattice volume, which would lead to increase in the filling limit, results in the production of no such precipitates. The chemical compositions of the SPS bulk samples obtained from the quantitative EDS analyses are summarized in Table 5.2. The point analyses were performed at more than 15 different grains and the average values were used. Note that here, we assume that Ga is located at both the void site and the Sb site with the ratio of 2:1 according to the previous study [30]. Room temperature values of the ρ, n_H, and μ_H are listed in Table 5.3, which are obtained from the Hall effect measurements. Here, the data for $CeFe_{3.5}Co_{0.5}Sb_{12}$ [31] are shown for comparison. With increasing x in $Ga_xCeFe_{3.5}Co_{0.5}Sb_{12-x/3}$, the n_H decreases, while the μ_H increases slightly. It is considered that the charge compensation occurs in the present case, because Ga in the void site would donate one electron while Ga in the Sb site would donate two holes [26]. Thus, the decrease in the n_H is due to the increase in the Ce content in the skutterudite phase. Actually, as can be confirmed through the quantitative EDS analysis (Table 5.2), the Ce content increases with increasing x in $Ga_xCeFe_{3.5}Co_{0.5}Sb_{12-x/3}$. On the other hand, the μ_H values increase slightly with increasing x, which is probably due to the decrease in the carrier-carrier scattering caused by the decreased n_H at high carrier concentration region over 10^{20} cm^{-3}.

The temperature dependences of σ, S, and $S^2\sigma$ of the SPS bulk samples are shown in Figures 5.3(a), 5.3(b), and 5.3(c), respectively. The literature data for $CeFe_{3.5}Co_{0.5}Sb_{12}$ [31] are shown for comparison. The σ values increase gradually with increasing x in $Ga_xCeFe_{3.5}Co_{0.5}Sb_{12-x/3}$, except for x = 0.21. The S values of all samples indicate positive values, i.e. the samples are *p*-type. As can be expected from the variation of the n_H, the S values increase with increasing x. Moreover, the S of all samples shows positive temperature dependence while the σ shows negative one, indicating a typical behavior for degenerated semiconductors. In particular, the present samples show slightly higher S values than the Ce single-filled ones, leading to higher power factor.

As a result, the sample with $x = 0.15$ shows the maximum power factor of 2.9 mW/mK^2 at 756 K.

Figure 5.3(d) and 5.3(e) show the temperature dependences of κ and κ_{lat} for the SPS bulk samples, respectively. We evaluated the κ_{lat} using the Wiedemann-Franz law ($\kappa_{el} = L\sigma T$), where L is the Lorenz number ($L = 2.45 \times 10^{-8}$ WΩK^{-2}). The literature data for $CeFe_{3.5}Co_{0.5}Sb_{12}$ [31] are shown for comparison. The κ shows rather flat temperature dependence, while the κ_{lat} slightly decreases with temperature. The κ_{lat} decreases with increasing x in $Ga_xCeFe_{3.5}Co_{0.5}Sb_{12-x/3}$ except for $x = 0.21$. The minimum κ_{lat} value is ~0.59 Wm^{-1}K^{-1} at 756 K obtained for the sample with $x = 0.15$, which is almost similar with the minimum value reported so far for Ce single-filled *p*-type skutterudites. This significant reduction in the κ_{lat} is due to the effective phonon scattering by both rattling of Ce and Ga in the void sites and substituted Ga at the Sb site.

The zT values of the SPS bulk samples calculated from the measured TE properties are shown in Fig. 5.3(f). The zT values of the samples except for the sample with $x = 0.06$ are higher than those of the literature data of Ce-single filled *p*-type skutterudites $CeFe_{3.5}Co_{0.5}Sb_{12}$ [31]. The results show that Ga co-filling into Ce-filled *p*-type skutterudites is effective for enhancement of zT. The sample with $x = 0.15$ exhibits the maximum zT of ~0.85 at 756 K.

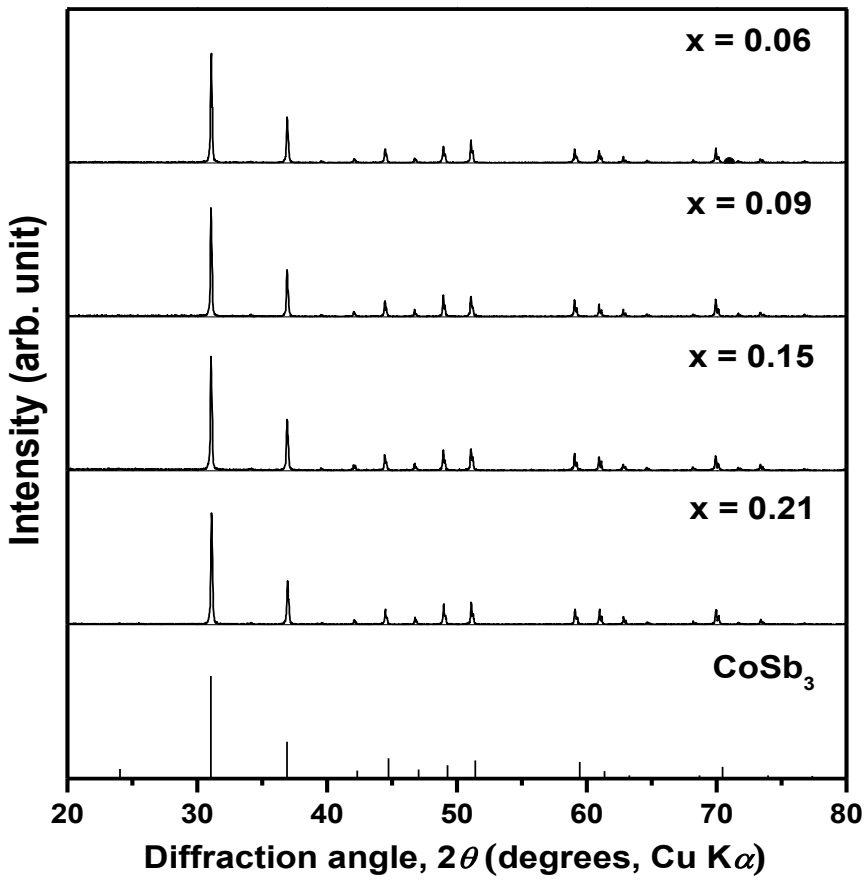

Fig. 5.1. Powder XRD patterns of the bulk samples of $Ga_xCeFe_{3.5}Co_{0.5}Sb_{12-x/3}$ (x = 0.06, 0.09, 0.15, and 0.21).

Table 5.1. Lattice parameter of the skutterudite phase and density of the bulk samples of $Ga_xCeFe_{3.5}Co_{0.5}Sb_{12-x/3}$ (x = 0.06, 0.09, 0.15, and 0.21).

Nominal composition	Lattice parameter (nm)	Density ($g \cdot cm^{-3}$)		Relative density (% T.D)
		Theoretical	Experimental	
$Ga_{0.06}CeFe_{3.5}Co_{0.5}Sb_{11.98}$	0.9105(4)	8.01	7.97	99
$Ga_{0.09}CeFe_{3.5}Co_{0.5}Sb_{11.97}$	0.9114(5)	8.02	7.69	96
$Ga_{0.15}CeFe_{3.5}Co_{0.5}Sb_{11.95}$	0.9118(2)	8.03	7.88	98
$Ga_{0.21}CeFe_{3.5}Co_{0.5}Sb_{11.93}$	0.9113(3)	8.05	7.93	99

Table 5.2. Chemical compositions at the skutterudite phase regions of the SPS bulk sample with nominal compositions of $Ga_xCeFe_{3.5}Co_{0.5}Sb_{12-x/3}$ (x = 0.06, 0.09, 0.15, and 0.21). The chemical composition is determined by the quantitative EDS analysis, where all the data are the average values obtained by repeating the point analyses at least 20 times.

Nominal composition	Results of the quantitative EDS analysis (at. %)					Chemical composition
	Ga	Ce	Fe	Co	Sb	
$Ga_{0.06}CeFe_{3.5}Co_{0.5}Sb_{11.98}$	0.3±0.1	5.5±0.4	21.0±0.7	3.0±0.4	70.3±0.9	$Ga_{0.05}Ce_{0.86}Fe_{3.49}Co_{0.51}Sb_{11.97}$
$Ga_{0.09}CeFe_{3.5}Co_{0.5}Sb_{11.97}$	0.3±0.2	5.6±0.7	21.1±1.1	2.9±0.7	70.2±1.7	$Ga_{0.07}Ce_{0.88}Fe_{3.50}Co_{0.50}Sb_{11.95}$
$Ga_{0.15}CeFe_{3.5}Co_{0.5}Sb_{11.95}$	0.4±0.1	5.6±0.3	21.1±0.4	2.9±0.3	70.1±1.1	$Ga_{0.11}Ce_{0.89}Fe_{3.51}Co_{0.49}Sb_{11.94}$
$Ga_{0.21}CeFe_{3.5}Co_{0.5}Sb_{11.93}$	0.5±0.2	5.5±0.5	21.0±0.6	3.0±0.5	70.1±0.8	$Ga_{0.12}Ce_{0.88}Fe_{3.49}Co_{0.51}Sb_{11.92}$

Table 5.2. Electrical resistivity ρ, carrier concentration n_H, and Hall mobility μ_H of the bulk samples of $Ga_xCeFe_{3.5}Co_{0.5}Sb_{12-x/3}$ (x = 0.06, 0.09, 0.15, and 0.21). All the data are obtained at room temperature. The data for $CeFe_{3.5}Co_{0.5}Sb_{12}$ [31] and $CeFe_3CoSb_{12}$ [26] are shown for comparison.

Nominal composition	ρ ($10^{-4}\Omega$cm)	n_H (10^{20}cm^{-3})	μ_H (cm^{2}V^{-1}s^{-1})
$Ga_{0.06}CeFe_{3.5}Co_{0.5}Sb_{11.98}$	7.8	2.3	44
$Ga_{0.09}CeFe_{3.5}Co_{0.5}Sb_{11.97}$	7.1	2.1	48
$Ga_{0.15}CeFe_{3.5}Co_{0.5}Sb_{11.95}$	6.7	2.0	50
$Ga_{0.21}CeFe_{3.5}Co_{0.5}Sb_{11.93}$	7.6	2.1	48
$CeFe_{3.5}Co_{0.5}Sb_{12}$ [31]	7.0	2.0	49
$CeFe_3CoSb_{12}$ [26]	7.7	2.7	-

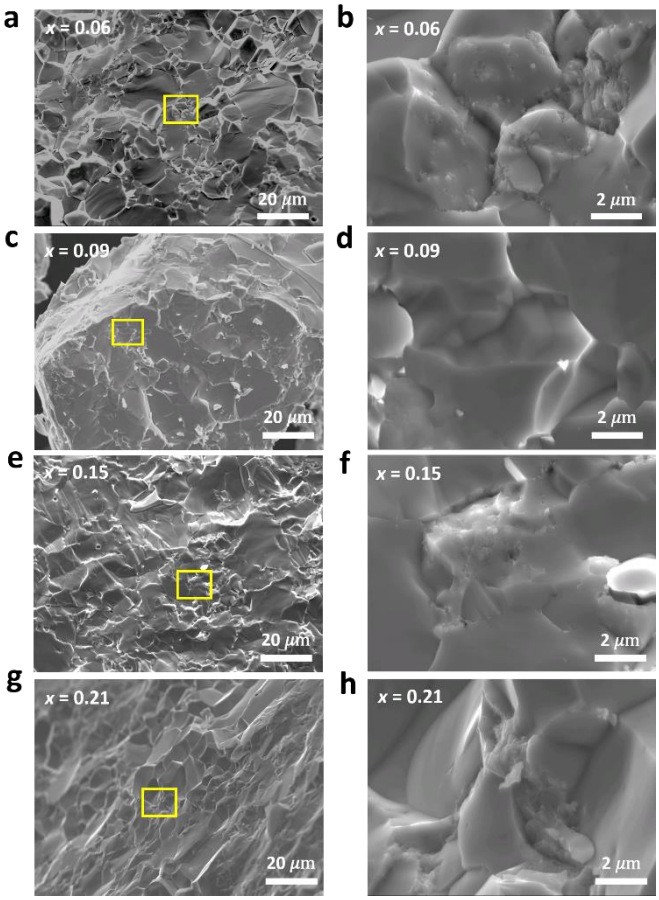

Fig. 5.2. FE-SEM images of the broken surface of the bulk samples of $Ga_xCeFe_{3.5}Co_{0.5}Sb_{12-x/3}$ (x = 0.06, 0.09, 0.15, and 0.21). (b), (d), (f), and (h) are the magnified images of the yellow regions in (a), (c), (e), and (g), respectively.

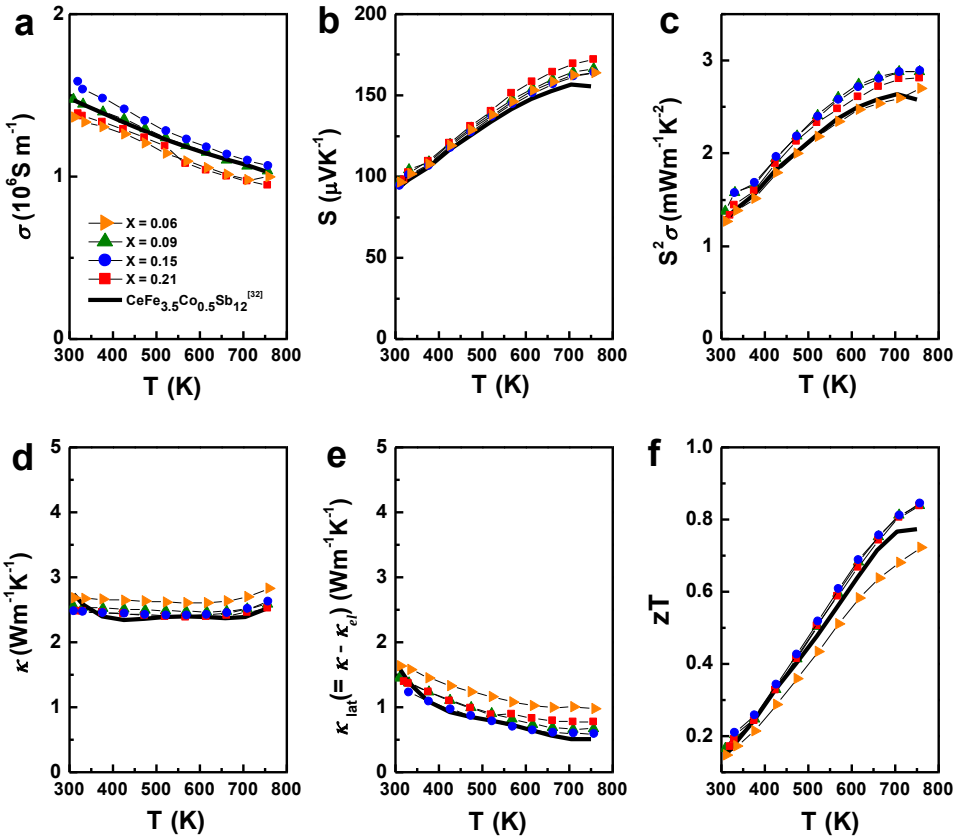

Fig. 5.3. Temperature dependences of the (a) electrical conductivity σ, (b) Seebeck coefficient S, (c) power factor $S^2\sigma$, (d) total thermal conductivity κ, (e) lattice thermal conductivity κ_{lat} ($=\kappa_l - \kappa_{l\,el}$), and (f) zT for the bulk samples of $Ga_xCeFe_{3.5}Co_{0.5}Sb_{12-x/3}$ (x = 0.06, 0.09, 0.15, and 0.21). The literature data for $CeFe_{3.5}Co_{0.5}Sb_{12}$ [31] are shown for comparison.

5.3 Conclusions

The effect of Ga and Ce co-filling on the TE properties of *p*-type skutterudites $Ga_xCeFe_{3.5}Co_{0.5}Sb_{12-x/3}$ (x = 0.06, 0.09, 0.15, and 0.21) were studied. Dense samples of $Ga_xCeFe_{3.5}Co_{0.5}Sb_{12-x/3}$ were obtained through a solid-state reaction followed by SPS. Under the assumption that Ga is located at both the void site and the Sb site with the ratio of 2:1, the charge compensation should occur which results in a constant carrier concentration regardless of different x in $Ga_xCeFe_{3.5}Co_{0.5}Sb_{12-x/3}$. Nevertheless, the hole carrier concentration decreases slightly with increasing x, which is due to the increase in the Ce content in the skutterudite phase. The present

samples showed higher power factor than the Ce single-filled system due to the optimized carrier concentration. The κ_{lat} decreases with increasing x due to the rattling effect of double-filled Ga and Ce and alloying effect by substituted Ga with the Sb site. As a result, even though the present samples are *p*-type ones, they show very nice zT values, 0.84 in maximum at 756 K for the sample with $x = 0.15$, higher than the best value obtained for the Ce single-filled *p*-type skutterudites.

5.4 References

[1] G. Snyder, E. Toberer *Nat. Mater.* **7**, 105 (2008).

[2] W. Liu, Q. Jie, H. S. Kim, and Z. Ren *Acta Mater.* **87**, 357 (2015).

[3] C. Vineis, A. Shakouri, A. Majumdar, and M. Kanatzidis *Adv. Mater.* **22**, 3970 (2010).

[4] W. Liu, X. Yan, G. Chen, and Z. Ren *Nano Energy* **1**, 42 (2012).

[5] S. Bhattacharya, A. Pope, R. Littleton, and T. Tritt *Appl. Phys. Lett.* **77**, 16 (2000).

[6] W. Li, S. Lin, M Weiss, Z. Zhen, J. Li, Y. Xu, W. Zeier, and Y. Pei *Adv. Energy Mater.* 1800030 (2018).

[7] B. Sales, D. Mandrus, B. Chakoumakos, V. Keppens, and J. Thompson *Phys. Rev. B* **56**, 23 (1997).

[8] G. Nolas, D. Morelli, and T. Tritt *Annu. Rev. Mater. Sci.* **29**, 89 (1999).

[9] F. Duan, L. Zhang, J. Dong, J. Sakamoto, B. Xu, X. Li, and Y. Tian *J. Alloys Compd.* **639**, 68 (2015).

[10] R. Carlini, A. Khan, R. Ricciardi, T. Mori, and G. Zanicchi *J. Alloys Compd.* **655**, 321 (2016).

[11] S. Lee, K. Lee, Y. Kim, H. Kim, G. Snyder, S. Baik, and S. Kim *Acta Mater.* **142**, 8 (2018).

[12] X. Shi, J. Yang, J. Salvador, M. Chi, J. Cho, H. Wang, S. Bai, J. Yang, W. Zhang, and L. Chen *J. Am. Chem. Soc.* **133**, 7837 (2011).

[13] C. Sekine, T. Ishizaka, K. Nishine, Y. Kawamura, J. Hayashi, K. Takeda, H. Gotou, and Z. Hiroi *Phys. Proc.* **75**, 383 (2015).

[14] L. Xi, J. Yang, W. Zhang, L. Chen, and J. Yang *J. Am. Chem. Soc.* **131**, 15 (2009).

[15] K. Kurosaki, G. Li, Y. Ohishi, H. Muta and S. Yamanaka, *Front. Chem.* **2**, 84 (2014).

[16] D. Zhao, H. Geng, and X. Teng *Intermetallics* **26**, 31 (2012).

[17] V. Khovaylo, T. Korolkov, A. Voronin, M. Gorshenkov, and A. Burkov *J. Mater. Chem. A* **5**, 3541 (2017).

[18] J. Kim, S. Choi, Y. Ohishi, H. Muta, S. Yamanaka, M. Takahashi, J. Tanaka, and K. Kurosaki

Mater. Trans. **58**, 8 (2017).

[19] D. Thompson, C. Liu, J. Yang, J. Salvador, D. Haddad, N. Ellison, R. Waldo and J. Yang, *Acta Mater.* **92**, 152 (2015).

[20] J. Peng, J. Yang, X. Song, Y. Chen, and T. Zhang *J. Alloys Compd.* **426**, 7 (2006).

[21] K. Wei, Y. Dong, P. Puneet, T. Tritt, and G. Nolas *J. Alloys Compd.* **614**, 330 (2014).

[22] S. Choi, K. Kurosaki, A. Yusufu, Y. Ohishi, H. Muta, and S. Yamanaka *J. Electoron. Mater.* **44**, 6 (2015).

[23] G. Tan, S. Wang, H. Li, Y. Yan, X. Tang *J. Solid State Chem.* **187**, 316 (2012).

[24] C. Zhou, D. Morelli, X. Zhou, G. Wang, and C. Uher *Intermetallics* **19**, 1390 (2011).

[25] T. Dahal, H. Kim, S. Gahlawat, K. Dahal, Q. Jie, W. Liu, Y. Lan, K. White, and Z. Ren *Acta Mater.* **117**, 13 (2016).

[26] J. P. Gonjal, P. Vaqueiro, C. Nuttall, R. Potter, and A. V. Powell *J. Alloys Compd.* **695**, 3598 (2017).

[27] X.Tang, L. Chen, T. Goto and T. Hirai, *J. Mater. Res.* **16**, 3 (2001).

[28] Y. Qiu, L. Xi, X. Shi, P. Qiu, W. Zhang, L. Chen, J. Salvador, J. Cho, J. Yang, Y. Chien, S. Chen, Y. Tang, and G. Snyder *Adv. Funct. Mater.* **23**, 3194 (2013).

[29] Y. Qiu, J. xing, X. Gao, L. Xi, X. Shi, H. Gu, and L. Chen *J. Mater. Chem. A* **2**, 10952 (2014).

[30] S. Choi, K. Kurosaki, G. Li, Y. Ohishi, H. Muta, S. Yamanaka, and S. Maeshima *AIP Adv.* **6**, 125015 (2016).

[31] L. Xi, Y. Qiu, S. Zhen, X. Shi, J. Yang. L. Chen, D. Singh, J. Yang, and W. Zhang *Acta Mater.* **85**, 112 (2015).

[32] J. Kim, Y. Ohishi, H. Muta, K. Kurosaki *AIP Adv.* 8, 105104 (2018).

[33] Y. Yan, W. Wong-Ng, L. Li, I. Levin, J. Kaduk, M. Suchomel, X. Sun, G. Tan and X. Tang, *J. Solid State Chem.* **218**, 221 (2014).

[34] D. Morelli and G. Meisner, *J. Appl. Phys.* **77**, 377 (1995).

CHAPTER VI

Summary and Discussion

In the present study, we investigated about *p*-type $CoSb_3$ based skutterudite compounds as bulk TE materials to improve TE performance. In particular, in order to synthesis for *p*-type TE materials, Co elements substituted with Fe elements, which is expected to not only enhance the electrical properties by optimization of carrier concentration but reduce the lattice thermal conductivity caused by point defect. In addition, we introduced various filling elements (such as In, Ce, and Ga) into the void site for reduction of lattice thermal conductivity due to the rattling effect caused by fluctuation of introduced filler atoms. And also, we attempted to optimize the carrier concentration tuning the ratio of filling elements (In, Ce, and Ga)/substitution element (Fe) for enhance the electrical properties. The results that were obtained this study are summarized as follow:

1) In chapter III, we confirmed that the maximum filling fraction limits of In as filling element in $In_xFeCo_3Sb_{12}$ system is to be less than 0.43 from the results of XRD and FE-SEM/EDS analysis. Also, we confirmed that excess In promoted the grain growth and generation of precipitate such as InSb. However, generated precipitates did not act a big role on phonon scattering, inversely, led to reduced electrical properties because they did not participate the reduction of carrier concentration. Thus, we could confirm that it can't be expected to enhance the TE properties due to the precipitates generated during the synthesis process. As a result, we could reduce the lattice thermal conductivity and improve the power factor due to the rattling effect and carrier concentration control caused by introduced In.

2) In chapter IV, we investigated the effect of Ce as filler and Fe as substation element on TE properties. In particular, we tried to find the optimum carrier concentration by tuning the Fe/Co. In this study, we could obtain almost single phase sample for all composition, thus precipitates did not greatly affect for TE properties. We could optimize the carrier concentration by tuning the Fe/Co and confirm that the optimum chemical composition is $y = 3.5$. Although the lattice thermal conductivity reduced with Ce, we confirmed that substituted Fe is more predominant than Ce filling for lattice thermal conductivity reduction. As a result, we could enhance the electrical properties by optimizing of chemical composition and reduce the lattice thermal conductivity by introduced Ce and substituted Fe. However, to identify specific reason for the effects of substituted Fe on the reduction of lattice thermal conductivity, we need to do follow-up research such as modeling.

3) In chapter V, we try to enhance the TE properties of Ce-filled $(Co, Fe)Sb_3$ by co-filling of Ga. Because there were reports about that Ga can occupy not only void site but also Sb site with the ratio 2:1, we tried to confirm the behavior of Ga in skutterudite phase. And also, we expected

that the reduction of lattice thermal conductivity due to the Ga, Ce co filling. The expected reduction of lattice thermal conductivity caused by the double (Ga and Ce) filling was not significant, however, we could improve power factor by optimization of carrier concentration. As a result, even though the present samples are *p*-type ones, we could obtain very nice *zT* value 0.84.

Figure 6.1 shows the figure of merit *zT* of (In, Ce and Ga)-filled skutterudites. And also, the right figure indicated the effect of each factor for figure of merit *zT* values. Number 1 shows the effects of single phase, small size grains and small amounts filler due to the filler elements. And number 2 shows the effect of charge compensation due to the large amounts filler atom. Also, number 3 shows the effect of optimization of chemical composition by doping control due to the changing of ration with Fe/Co and filler atom. Finally, number 4 shows the effect of dual site occupancy of Ga with Sb site and void site in skutterudite. As a results, I attempted to enhance the TE properties of $(Fe,Co)Sb_3$, I could obtain the sample with best TE performance through the using these methods.

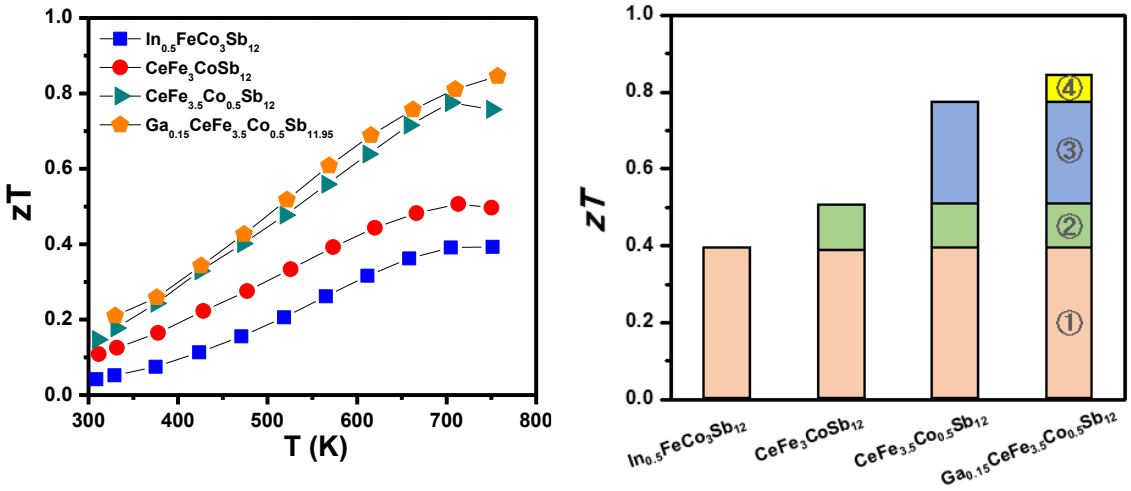

Fig. 6.1. Figure of merit *zT* of (In, Ce, Ga)-filled skutterudites with best chemical composition.

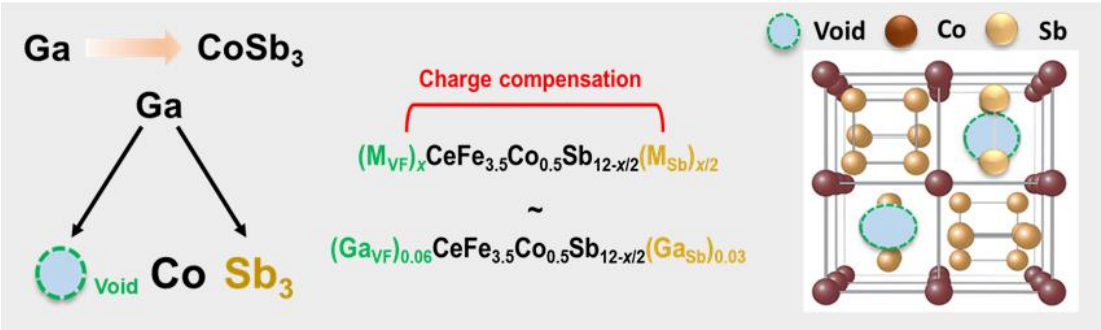

Fig. 6.2. Schematic image of dual site occupancy of Ga in skutterudite.

In this thesis, I firstly applied the concept of dual site occupancy for Ga element to *p*-type (Fe,Co)Sb_3 TE materials as shown in Figure 6.2. And also, I could improve TE properties of *p*-type TE materials, and confirmed that this method is effective for enhancement of TE performance, moreover, I could optimize the chemical composition of (Fe,Co)Sb_3 skutterudite compounds using the various method as shown in figure 6.3.

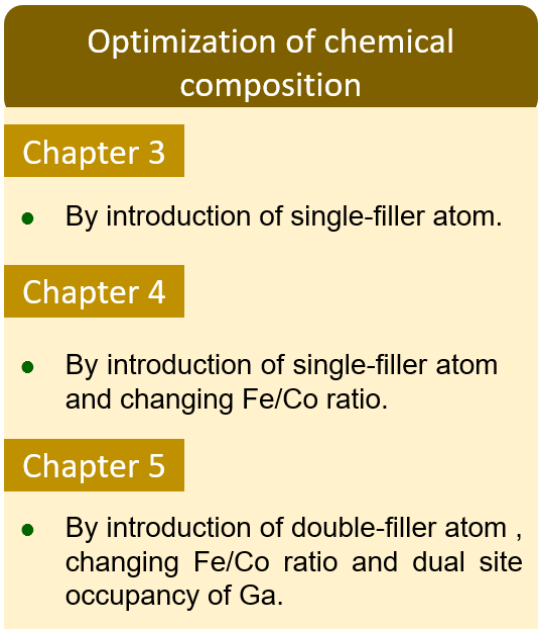

Fig. 6.3. Strategies to improve TE performance for *p*-type TE materials.

Finally, through these studies, I confirmed that the carrier density control by optimizing of chemical composition and rattling effect by introducing of filler could be effective way to enhance the TE properties of bulk TE materials such as skutterudites. I expect these results to help develop other TE materials, and also I expect that the problems of energy crisis or environmental pollution will be resolved gradually through commercialization of TE materials.

Research Achievements

List of Publications

Research Articles

1. Thermoelectric Properties of $In_xFeCo_3Sb_{12}$ Consisting Mainly of In-Filled *p*-type Skutterudites.
   Materials Transactions **58**, 1207-1211 (2017).
   Jungmin Kim, Ken Kurosaki, Seongho Choi, Yuji Ohishi, Hiroaki Muta, Shinsuke Yamanaka, Misato Takahashi, and Junya Tanaka.
2. Enhancement of Thermoelectric Properties of *p*-type Single-Filled Skutterudites $Ce_xFe_yCo_{4-y}Sb_{12}$ by tuning the Ce and Fe content.
   AIP Advances **8**, 105104 (2018).
   Jungmin Kim, Yuji Ohishi, Hiroaki Muta, and Ken Kurosaki.
3. Enhanced Thermoelectric Properties of Ga and Ce Double-Filled *p*-type Skutterudites.
   Materials Transactions. (Submit)
   Jungmin Kim, Yuji Ohishi, Hiroaki Muta, and Ken Kurosaki.

List of Presentations

International Conference

1. Thermoelectric Properties of Ce-Filled *p*-type Skutterudites: $Ce_xFe_yCo_{4-y}Sb_{12}$.
   2107 MRS Fall Meeting & Exhibit, Boston, USA, Nov 26 – Dec 1, (2017).
   Jungmin Kim, Yuji Ohishi, Hiroaki Muta, and Ken Kurosaki.

Domestic Conference

2. Thermoelectric Properties of Ce-Filled *p*-type Skutterudites: $Ce_xFe_yCo_{4-y}Sb_{12}$.
   14th TSJ Meeting, Osaka, Japan, Sep 11 - 13, (2017).
   Jungmin Kim, Yuji Ohishi, Hiroaki Muta, and Ken Kurosaki.
3. Thermoelectric Properties of Ce-Filled *p*-type Skutterudites: $Ce_xFe_yCo_{4-y}Sb_{12}$.
   2018 JSPM Autumn Meeting, Niigata, Japan, Oct 30 - 31, (2018).
   Jungmin Kim, Yuji Ohishi, Hiroaki Muta, and Ken Kurosaki.

Acknowledgements

I would like to express my deepest gratitude to my supervisor, Associate Professor Dr. Ken Kurosaki for his excellent guidance, caring, patience and providing me with an excellent atmosphere for doing research which kept me motivated throughout my PhD. I am also thankful for Associate Professor Dr. Hiroaki Muta and Associate Professor Dr. Yuji Ohishi. They gave me many helpful guidance and great advices on the present thesis. My sincere thank is expressed to the thesis committee, Professor Dr. Kitada Takanori and Professor Dr. Yamamoto Takao for their helpful suggestions on the present thesis.

I would especially like to thank to Dr. Sungho Choi and Dr. Kyungmin Ok for kind discussion and support of experiment. He was help to my start in the lab. We had a discussion about solving the research or academic problem about thermoelectric properties of materials as well as *p*-type filled (Fe,Co)Sb_3-based skutterudites. Without their help, I would not have complete my PhD.

My thankfulness is also extended to all members in the Yamanaka Laboratory for their helpful advice and encouragement in the life of a Ph.D. student.

My deep gratitude goes to my mother, Jungran An and my sister Hyoi Kim. They give me never-ending care and understanding, while leaving me with great freedom of achieving my dreams. Without their love, I could not have gone so far. Without any doubt, I dedicate this thesis to my family.

February 2019

Jungmin Kim